Carbon Impurity Minimization of Solution-Processed, Thin-Film Photovoltaics via Ligand Engineering of CuInS₂ Nanoparticles

Daniel C. Hayes, Samantha A. Langdon, Robert M. Spilker, Rakesh Agrawal*

Davidson School of Chemical Engineering, Purdue University, 480 Stadium Mall Dr., West

Lafayette, IN, USA

Colloidal nanoparticles, ligand chemistry, solution-processing, thin-film, solar cell, carbon impurities

Abstract:

Colloidal semiconductor nanoparticles have long been used as a reliable method for depositing thin films of semiconductor materials for applications such as photovoltaics via solution-processed means. Traditional methods for synthesizing colloidal nanoparticles often utilize heavy, long-chain organic species to serve as surface ligands which, during fabrication of selenized chalcogenide films, leaves behind an undesirable carbonaceous residue in the film. In an effort to minimize these residues, this work looks at using N-methyl-2-pyrrolidone (NMP) as an alternative to the traditional species used as surface ligands. In addition to serving as a primary ligand, NMP also serves as the reaction medium and coating solvent for fabricating CuInS₂ (CIS) nanoparticles and thin-film solar cells. Through the use of the NMP-based synthesis, a substantial reduction in carbonaceous residues was observed in selenized films. Additionally, the resulting fine-grain layer at the bottom of the film was observed to exhibit a larger average grain size and increased chalcopyrite character over that of traditionally prepared films, presumably as a result of the reduced carbon content. As a result, a gallium-free CuIn(S,Se)2 device was shown to achieve power-conversion efficiencies of over 11% as well as possessing exceptional carrier generation capabilities with a short-circuit current density (J_{SC}) of 41.6 mA/cm² which is among the highest for the CIGSSe family of devices fabricated from solution-processed methods.

Introduction:

Thin-film photovoltaics are typically fabricated via physical vapor-deposition (PVD) or solution-deposition methods, each of which possesses its own unique advantages. For example, the PVD route is typically chosen for more robust material systems in which the ability to deposit high purity material with great control over deposition parameters, allowing for the deliberate tuning of a film's properties based on its material composition, is desired. This level of fine tunability is essentially required for achieving the highest efficiencies as we see in Cu(In,Ga)(S,Se)₂ (CIGSSe) solar cells, with the former record at a power conversion efficiency (PCE) of 23.35%, having the CIGSSe absorber layer produced via DC-magnetron sputtering followed by annealing in selenium- and sulfur-containing atmospheres. We should mention the record has recently been improved to 23.6%, although experimental details have yet to be conveyed in the literature.² The advantages that the PVD method provides, however, are not without their drawbacks. This route primarily uses complex, and therefore expensive, deposition equipment, which generates high capital costs. Additionally, due to the nature of the ultra-high vacuum processing equipment and the time required to complete a full vacuum cycle, sample throughput is inherently low. In order to rectify this, solution-processing of thin-film solar cell absorbers has been extensively studied as a viable alternative.³

Solution processing of CIGSSe covers numerous chemistries including water-,^{4–6} alcohol-,^{7,8} hydrazine-,^{9–11} amine-thiol-,^{12–14} and colloidal nanoparticle-based^{15–18} to name a few. The current record solution-processed CIGSSe device stands at a certified 17.3% efficiency and is fabricated using the hydrazine method¹¹—notable because hydrazine is particularly well-suited for ink formulations. Consisting of only nitrogen and hydrogen, it decomposes into volatile components

that won't leave any residues. Unfortunately, hydrazine, with its explosive and toxic properties, would face numerous safety challenges in the scale-up of such a process.

Among the alternatives to the hydrazine method, the colloidal nanoparticle method provides enhanced tunability in terms of the potential for different precursor and solvent choices during film fabrication. Synthesis of colloidal nanoparticles provides a method for fabricating building blocks of a desired material, such as Cu(In,Ga)S₂ (CIGS), in solution from a wide array of commercially available precursors, providing a means for convenient post-synthesis use of the synthesized materials. For solution-based, thin-film fabrication, these nanoparticles are subsequently resuspended in a solvent suitable for creating a stable suspension at high concentrations, thus providing an efficient method for film deposition. In order to obtain nanoparticles that suspend well, a high degree of surface passivation, provided by the ligand, and a solvent that allows for a high degree of solvation of the ligand species are simultaneously required to reduce surface energies enough to prevent particle agglomeration and flocculation. This surface passivation can include various organic and inorganic species, so long that they can bind to surface atoms (similar to a ligand-metal bond in a coordination complex). 19 The functionalization of the surface can vary greatly depending on what ligands are used ranging from long-chain species like oleylamine (OLA)^{15,18,20} or trioctylphosphine oxide (TOPO)²¹ to various inorganic species^{17,22–25}. This surface functionality then determines the type of solvents that can be used (polar vs. nonpolar) to formulate colloidal inks from the nanoparticles. In addition to adequate surface passivation, nanoparticle size must also be considered, as particles too large in size are overcome by gravitational forces, causing sedimentation.

While species like OLA and TOPO have long been used in the literature as a reliable ligand choice, ²⁶ they leave behind large amounts of carbonaceous residues when used in film fabrication.

This is especially noticeable during selenization of sulfur-containing chalcogenides like CIGS or Cu₂ZnSnS₄ (CZTS). Here, vapor selenium condenses on the sulfide film, and percolates its way through the film while reacting with the sulfide material to form the selenide material. As the Se front makes its way through the film, a rejected carbon front forms and begins to move with the Se, and increases in thickness as the selenization proceeds. This type of growth continues until an equilibrium is met between competing mass transfer effects and chemical reactivities to leave behind the fine-grain layer.²⁷ This fine-grain layer has long been studied in solution-processed photovoltaics, with many describing it as an undesirable consequence of solution-processed film fabrication leading to a higher recombination risk resulting from the lack of long-term crystal order and high number of grain-grain interfaces. 17,27-31 These residues are shown to affect morphological aspects of films 13,17,27,28 as well as elemental distributions, 17,29 leaving unintended compositional variations including a bulk composition that differs from that of the coating ink, and most consequently, intended composition. Others argue that carbon might create a better ohmic contact between the Mo and the coarse-grained material in CZTSSe, but this conclusion was reached using devices with substantially different morphologies, indicating other factors may be at play.³² Listed in **Table S1** is a non-exhaustive summary of some examples of solution-processed CIGSSe devices describing the thickness of their fine-grain layers, fabrication methods, and resulting performance metrics. We urge the reader to interpret this table with caution as many other parameters can contribute to the performance of solution-processed photovoltaics, including fine-grain elemental composition, morphology and grain boundary composition of the coarse grains, and interface quality between subsequent layers such as CIGSSe and CdS among many other reasons.

Reducing the overall carbon content in solution-processed thin-film devices is primarily motivated by the highest-efficiency CIGSSe devices being produced via the PVD^{1,33} or hydrazine¹¹

methods—both of which involve processes that avoid the deliberate usage of carbon-containing materials at any step during the absorber layer fabrication. The resulting film morphologies are thick, homogeneous, and coarse-grained—a trait believed to be crucial in reaching the high efficiencies that these devices achieve. In order to reduce the carbon content in solution-processed, thin-film devices, several techniques have been studied, including ligand-exchange strategies, ^{17,34} direct-synthesis procedures utilizing inorganic or smaller-chain ligands, ^{22,35,36} or via the sonochemical approach in which typical surfactants are also omitted. ^{37–40} Many of these alternate strategies, however, utilize methods that significantly increase fabrication complexity and material usage, especially for the ligand-exchange methods, or involve procedures that may have increased difficulties in scale-up due to less commonly used materials. While the sonochemical approach is attractive in that it can produce surfactant-free Cu(In_{1-x}Ga_x)(S_{1-y}Se_y)₂ nanoparticles under bulk, low-temperature conditions, some of these methods still require the use of toxic hydrazine or show limited device performance (<1% PCE) with all methods appearing to suffer from a high degree of particle agglomeration which may lead to difficulties when coating films.

In an effort to overcome these shortcomings and to provide a reliable method of producing stable, colloidal Cu(In,Ga)S₂ nanoparticles while minimizing carbon impurities in devices, we are proposing the use of N-methyl-2-pyrrolidone (NMP) as an alternate ligand. We believe NMP is a suitable candidate, in part, for its ability to bind strongly to Lewis acid sites⁴¹ and various metal species,⁴² especially transition metals,^{43–46} in coordination complexes. It has also been used to functionalize bulk materials, via methods like grinding and sonication in the presence of NMP to create dispersible materials for casting into a film.^{45–47} Although not a direct indication of ligand-binding strength, its volatility (boiling point (b.p.) ~ 202 °C) is much greater than that of traditional ligands like OLA (b.p. ~ 360-365 °C) which we attribute, in part, to its easier removal during film

fabrication and processing. Additionally, NMP is a commonly used solvent, not only in other research fields and applications, ^{41,48,49} but it is also widely used in many industrial applications, including hydrocarbon recovery in the petrochemical industry, drug production in the pharmaceutical industry, ⁵⁰ and electrode preparation in the fabrication of lithium-ion batteries, ⁵¹ to name a few. In this report, we propose a direct synthesis pathway of Cu(In_{1-x}Ga_x)S₂ colloidal nanoparticles using NMP as the reaction medium and primary surface ligand. To the best of our knowledge, NMP has seldom been used in the bottom-up synthesis of colloidal nanoparticles, ⁵² and this report serves as the first approach for its use in the synthesis of semiconductor nanoparticles for photovoltaic applications.

Experimental Methods:

Materials

Copper(I) sulfide (99.99%), copper(II) chloride (≥99.995%), copper(II) acetylacetonate (≥99.99%), indium(III) chloride (99.999%), gallium(III) acetylacetonate (≥99.99%), sulfur flakes (S; 99.99%), oleylamine (OLA; 70%, technical grade), *N*-methyl-2-pyrrolidone (NMP; 99.5%, anhydrous), 1,2-ethanedithiol (EDT; ≥98.0%), *n*-propylamine (PA; ≥99.0%), toluene (99.8%, anhydrous), acetonitrile (MeCN; 99.8%, anhydrous), and 1-hexanethiol (HT; 95%) were purchased from Sigma-Aldrich and used as received with the exception of OLA and NMP, which were degassed with successive freeze-pump-thaw cycles under argon. Copper(I) iodide (99.995%), gallium(III) chloride (99.999%), gallium(III) iodide (99.999%), indium(III) iodide (99.999%), isopropyl alcohol (IPA; 99.9%), and hexanes (99%, mixture of isomers) were purchased from Fisher Scientific and used as received. Indium powder (99.999%) was purchased from Strem Chemicals and used as received. Sodium fluoride (99.9%) was purchased from Stanford Advanced Materials and used as received.

Synthesis of CIGS Nanoparticles

All nanoparticle syntheses and precursor preparation steps were performed in a nitrogenfilled glovebox or in a sealed vessel that contained a nitrogen or argon headspace unless otherwise noted. Metal halide salts were dissolved or suspended as a slurry in NMP prior to use for synthesis. Stock solutions of these mixtures were prepared at a concentration of 0.8 M before mixing with sulfur solutions in PA or OLA. Final reaction concentrations were 0.0572 M w.r.t. In (or In + Ga) with 100% molar excess of sulfur. Further experimental details on nanoparticle syntheses are provided in the Supplementary Information section. After each reaction, synthesized nanoparticles underwent successive washing cycles, described as follows: syntheses with NMP utilized MeCN as the solvent and toluene as the antisolvent, while nanoparticle syntheses with OLA utilized hexane as the solvent and IPA as the antisolvent. The first wash involved the addition of antisolvent only to the reaction mixture in a ~3:1 antisolvent-to-reaction mixture ratio, followed by vortex mixing and then centrifugation for 5 min at 14,000 RPM and decanting of the resulting supernatant. This process was done at least two additional times using the respective solvents first to resuspend the synthesized nanoparticles and vortex mixing followed by addition of the antisolvents in a \sim 23:1 antisolvent-to-solvent ratio with additional vortex mixing and centrifugation. After the final wash, the nanoparticles were dried under Argon flow followed by vacuum and stored in a nitrogen-filled glovebox before further use.

Nanoparticle Ink Preparation and Film Coating

Dry nanoparticles were weighed and combined with the desired coating solvent to resuspend the nanoparticles for coating. NMP and HT were the solvents used for nanoparticles synthesized in NMP and OLA, respectively, at concentrations of 150 to 250 mg/mL. Upon solvent addition, the nanoparticles were dispersed using a bath sonicator for ~1 h at room temperature. Films were then

coated on Molybdenum-coated soda-lime glass (SLG) via a blade-coating procedure using a borosilicate glass rod as a blade and a modified 3D printer in a nitrogen-filled glovebox. For inks suspended in NMP, the print bed was held at a constant temperature of 100 °C, and two total passes of the coating rod over the film at a speed of 10 mm/s and a rod-film spacing of 100 µm above the film were used as coating conditions. After each coat, the film was allowed to dry for 2 min on the print bed, followed by a 1 min anneal at 250 °C on a hot plate. The film was then placed on aluminum fins to naturally cool for 1 min before being placed on an aluminum block, acting as a heat sink, to be thermally quenched between subsequent coatings. For inks suspended in HT, coatings were performed with the modified 3D printer in a nitrogen-filled glovebox with 2-3 total passes per coat. A rod-film spacing of 100 µm was used, and the film was annealed at 350 °C for 1 min between coatings. Coatings for NMP and HT inks were repeated between 5-12 times to achieve a film thickness of 1-2 µm.

Device Fabrication

Devices were constructed according to the SLG/Mo/CISSe/CdS/ZnO/ITO/Ag/MgF₂ substrate device architecture. Mo was deposited on SLG substrates via DC-magnetron sputtering to a thickness of 800 nm. Nanoparticles were coated next, as previously described. Once coated, 15 nm of NaF was deposited via thermal evaporation. The films then underwent a selenization procedure in a tubular furnace where the films were inserted into a graphite box with ~400 mg of Se pellets. Before being fully inserted, the furnace was purged of air using vacuum pump cycles and Ar to refill and allowed to heat to 500 °C, upon which the films were inserted to bake for 20 min. Ar flow was present during heat-up to continue purging the furnace, but no Ar flow was present during the 20 min the film was exposed to selenization conditions. ~50 nm of CdS was then deposited on the films via a chemical-bath deposition. Following CdS, 80 nm of ZnO and 220

nm of ITO were deposited via RF sputtering. Lastly, silver grids with a thickness of 200 nm were deposited via thermal evaporation followed by ~ 100 nm of MgF₂ via thermal evaporation to act as an anti-reflective coating.

Characterization

Raman spectra were collected using a Horiba/Jobin-Yvon HR800 Raman spectrometer with a 632.8 nm wavelength excitation laser. Powder X-ray diffraction (pXRD) data were collected using a Rigaku SmartLab diffractometer with a Cu K α ($\lambda = 1.5406$ Å) source operated at 40 kV / 44 mA in parallel-beam mode. Nuclear magnetic resonance (¹H NMR) spectroscopy were collected with a Bruker AV-III-400-HD using a relaxation time of 6 s and 32 scans. Scanning electron microscopy (SEM) images were taken using both an FEI Quanta 3d FEG dual-beam SEM with an Everhart-Thornley detector at an accelerating voltage between 5-15 kV and a working distance of 10 mm and a Thermo Scientific Helios G4 UX Dual Beam SEM with an Everhart-Thornley detector at an accelerating voltage of 5 kV and a working distance of 4 mm. Focused ion beam (FIB) etching was also performed on the Thermo Scientific Helios G4 UX Dual Beam SEM. Transmission electron microscopy (TEM) images were taken using a Tecnai G2 20 TEM with an accelerating voltage of 200 kV. Scanning transmission electron microscopy-energy dispersive x-ray spectroscopy (STEM-EDX) data and selected-area electron diffraction (SAED) images were collected on a Talos 200X TEM with an accelerating voltage of 200 kV. Current-voltage (J-V) measurements were performed using an Oriel Sol3A solar simulator with a temperature-controlled stage and AM1.5G filtering, calibrated with an Oriel 91150V silicon reference cell. These measurements were taken at 25 °C and 1000 W/m². External quantum efficiency (EQE) was measured at a chopper frequency of 155-160 Hz with a preamplifier used for signal processing. No external light biasing was used during EQE measurements.

Results and Discussion:

Nanoparticle Synthesis

Synthesis procedures of the CIS nanoparticles (NPs) was first investigated via the amine-thiol system which is capable of dissolving pure metals and metal chalcogenides.⁵³ These NPs were synthesized from Cu₂S and In metal mixtures, each dissolved in PA and EDT as described in the experimental section. Interestingly, NPs synthesized from the amine-thiol precursors in NMP primarily formed a highly crystalline wurtzite-phase CIS when synthesized at 200 °C using the Schlenk line setup. For $Cu(In_{1-x}Ga_x)(S_{1-y}Se_y)$ at all x and y values, the chalcopyrite crystal structure is the thermodynamically favored phase.⁵⁴ Increasing the temperature to 250 °C showed the continued presence of both wurtzite and chalcopyrite phases as seen from pXRD, but a visible preference to formation of the chalcopyrite phase is observed alongside larger NPs as denoted by the low FWHM in the pXRD (Figure S1). Attempts to suspend these larger nanoparticles were mostly ineffective, leading to poor film quality for coatings from such an ink. These resulting phases and level of crystallinity differ for NPs synthesized using amine-thiol precursors in OLA. In some of our previous works, ^{17,55} we see phase-pure chalcopyrite CIGS NPs with relatively broad peaks, indicating smaller particles. We believe this is caused by differences in the reaction mediums, creating potential differences due to different binding motifs and ligand size between OLA and NMP.

According to Tappan et al., the chalcogen source can impact the preferred crystal phase formed simply due to how readily available the chalcogen is based on the strength of existing carbon-chalcogen bonds in the precursor species.⁵⁶ For these reactions involving amine-thiol chemistry, the chalcogen source is EDT. To further investigate the impact of the sulfur source, elemental sulfur was added to the amine-thiol reaction to understand its impact on phase formation. The

addition of free sulfur was shown to favor the formation of chalcopyrite CIS, but wurtzite-CIS was still observed. The results of this and all previously discussed syntheses are shown in **Figure S1**.

In order to form NPs of the desired phase and size, an alternative reaction pathway utilizing metal chlorides and elemental sulfur was investigated. In this approach, CuCl₂, InCl₃, and sulfur dissolved in propylamine via its reactive dissolution pathway with primary amines⁵⁷—were added together to a reaction vessel with NMP. Upon heating to 250 °C for 90 minutes, NPs of the chalcopyrite phase of CIS were formed (XRD shown in Figure 1 and TEM shown in Figure S2). The synthesized particles interestingly appear to be NP clusters comprised of many smaller NPs which may be due to the small size of NMP as a ligand. Gallium-containing nanoparticles were also synthesized by substituting some InCl₃ with GaCl₃ for a GGI of 0.3 and 0.5. These synthesized nanoparticles are shown by their XRD patterns in Figure S3. While the chalcopyrite phase was shown to form for gallium-containing nanoparticles, it was observed that the CGI of the synthesized NPs was greater than the CGI measured in the precursor solutions. As shown in Figure S4, the precursor CGI had to be tuned to obtain a desired CGI in the synthesized NPs. Galliumcontaining NPs were also shown to aggregate more readily, leading to difficulties in producing device-quality films. These observations and associated difficulties are discussed further in the Supplementary Information. As a result, only CIS NPs were used for further characterization and device fabrication.

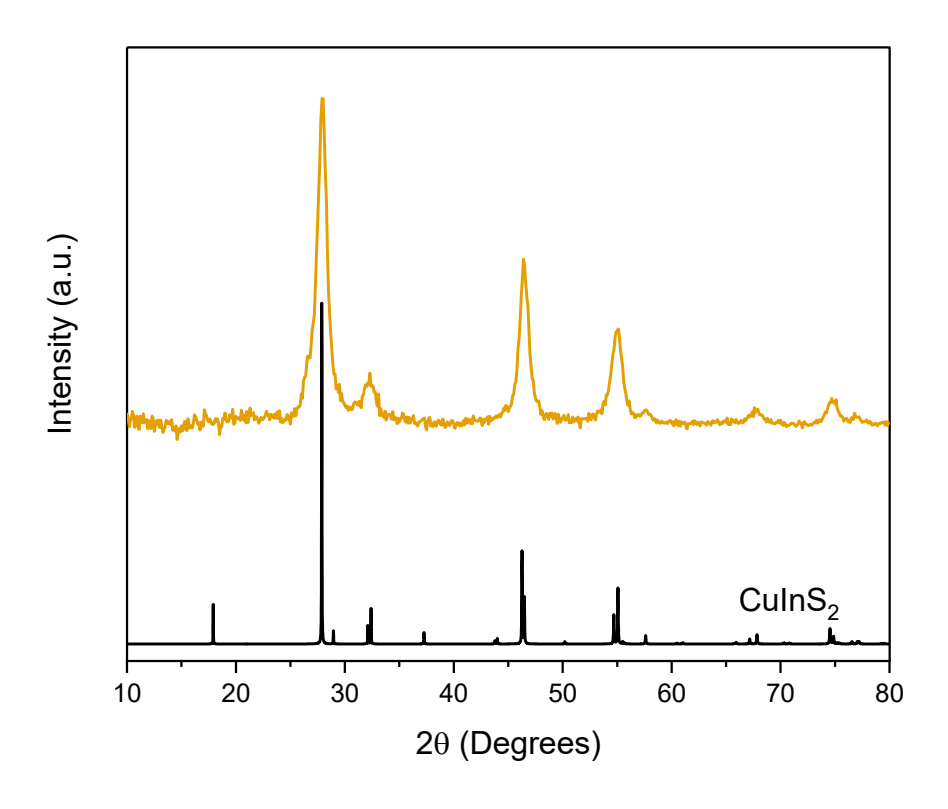


Figure 1. XRD diffraction pattern of synthesized CuInS₂ nanoparticles from the NMP route. The standard used is simulated from chalcopyrite CuInS₂ - ICSD# 66865.

In order to investigate the surface chemistry of the synthesized nanoparticles, ¹H NMR spectroscopy was utilized to determine which species were bound to the NP surfaces. In typical NMR with unbound species, complete freedom of mobility in solution is attainable which allows proper alignment upon exposure to the applied magnetic field during NMR spectroscopy. As a result, they typically exhibit very clear and distinct response, shown as sharp peaks in a spectrum, as these free species all share a very similar chemical environment with other molecules of the same species in solution. In the surface-bound species, on the other hand, the mobility of protons very close to the NP surface will be restricted, which inhibits total alignment in the applied magnetic field used in NMR spectroscopy, causing line broadening in ¹H NMR.⁵⁸ **Figure 2** shows

the ¹H NMR spectrum of nanoparticles synthesized via the metal chlorides. We chose DMSO-d₆ as our deuterated solvent of choice since it provided good solvation of the nanoparticles to create a stable suspension. Here, we see bound species, indicated by several very broad, overlapping peaks in two fairly distinct regions. With NMP being a substantially smaller molecule than OLA, and thus a much smaller ligand, significant line broadening is exhibited for all expected NMP resonances, due to their close proximity to the nanoparticle surface, by the broad peaks between 2-4 ppm. Additional broad peaks with notably lower FWHM are also shown between 0.5-2 ppm chemical shift that don't appear to match with or are too far shifted from any peaks from neat NMP. This likely indicates that the PA used during synthesis is also present in surface binding and passivation of the synthesized nanoparticles. This is not much of a surprise as primary amines have been shown to exhibit strong binding to CuInS₂ NP surfaces.⁵⁹ Because NMP and PA are both relatively small molecules, being bound to a nanoparticle surface will cause fairly significant line broadening for most, if not all, resonances in the ¹H NMR spectrum, making peak assignment and quantification measurements difficult. Additionally, while NMP typically shows binding to the oxygen site as a ligand in molecular species, 42,44,60 we cannot rule out that the lone pair from its nitrogen atom may be contributing as a site for nanoparticle surface binding, causing further peak broadening for nearby protons. In order to quantify or better assign these broad peaks, additional techniques, such as diffusion-ordered NMR spectroscopy or nuclear Overhauser effect spectroscopy may be needed.

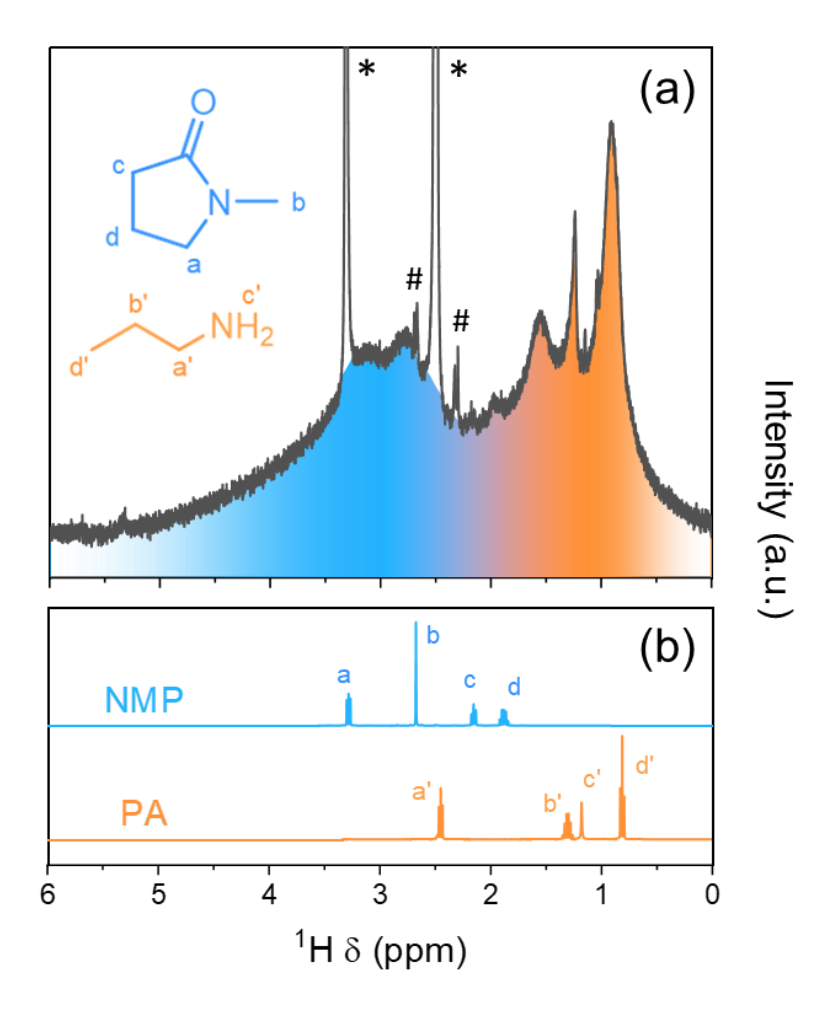


Figure 2. ¹H NMR spectra of NMP-CIS nanoparticles synthesized via metal chlorides (a) with measured standards of propylamine (PA) and NMP (b). Several broad peaks are shown indicating the presence of surface binding likely by both species. The regions we associate with surface-bound resonances primarily from NMP and PA are filled in with blue and orange, respectively. Peaks denoted with * are assigned to residual H2O in the deuterated solvent and DMSO at 3.3 and 2.5 ppm, respectively. Peaks denoted with # are a result of ¹³C satellite peaks from DMSO-d5 which are only visible because of the y-axis range required to appropriately view the low intensity resonances from the surface-bound species. All other resonances are assigned to NMP or PA residuals.

Film Fabrication

After the nanoparticle synthesis, thin films were fabricated by suspending the particles in a suitable solvent. The choice of solvent here is critical to prevent aggregation of the nanoparticles, leading to non-uniform coatings. Ideal solvents for nanoparticle suspensions should have characteristics similar to that of the surface-bound species, allowing for thorough solvation of the ligands. Since we've determined that NMP and PA are the dominant ligands, choosing a polar solvent like NMP seemed the proper choice for providing a stable suspension of NPs. Choosing NMP as the coating solvent also reduces the number of different processing components by utilizing the same species for three crucial components of the process—the reaction medium, surface ligand, and coating solvent—easing the path for the potential scale-up of such a process.

One of the key advantages to coating with NP inks over molecular precursor inks is that NP suspensions typically allow for much higher ink concentrations, leading to a much quicker and simpler coating process. Of course, the colloidal stability of the particles will greatly affect this, but with well-suspended NPs, mass concentrations of >200 mg/mL are commonly achievable. NP coatings can also be performed out of a variety of more user-friendly solvents. For the case of NMP, the print stage was set to 100 °C to dramatically increase the wettability of the solvent on the substrate used. Most solvents typically experience a decrease in surface tension with increases in temperature. As a result, the as-coated films exhibited a smooth profile as shown in the SEM image below in **Figure 3**.

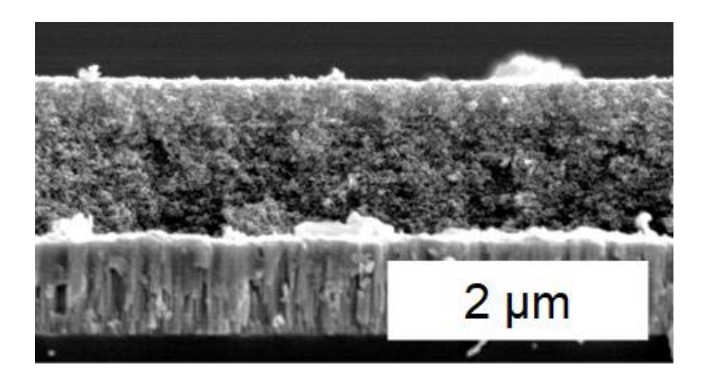


Figure 3. SEM cross-section of an as-coated CIS film showing smooth morphology achievable via these NMP-based nanoparticle inks.

To achieve device-ready films, a selenization is performed to achieve highly crystalline CuIn(S,Se)₂ thin films. NaF was deposited on films before selenization to incorporate sodium—crucial for enhanced grain growth and electronic properties of the film.⁶³ Selenization of an NMP-CIS film shows a bilayer morphology (shown in **Figure 4a**), typical of solution-processed sulfide films that undergo selenization. A top-down view is shown in **Figure S5**. An increased coarseness of this fine-grain layer is notable when compared to other films, ^{13,14,29} such as the more traditional OLA-nanoparticle film^{17,18,27} which produces a fine-grain layer with very small average grain size (shown in **Figure 4b**). Although still a fine-grain region in the NMP-CIS film, the observed enhanced growth indicates that the fine-grain region may also consist of chalcopyrite grains, albeit smaller in size, which would positively impact the performance of these films. This is different from traditionally prepared films in which the fine-grain region is typically rich in copper, carbon, and selenium.^{17,29}

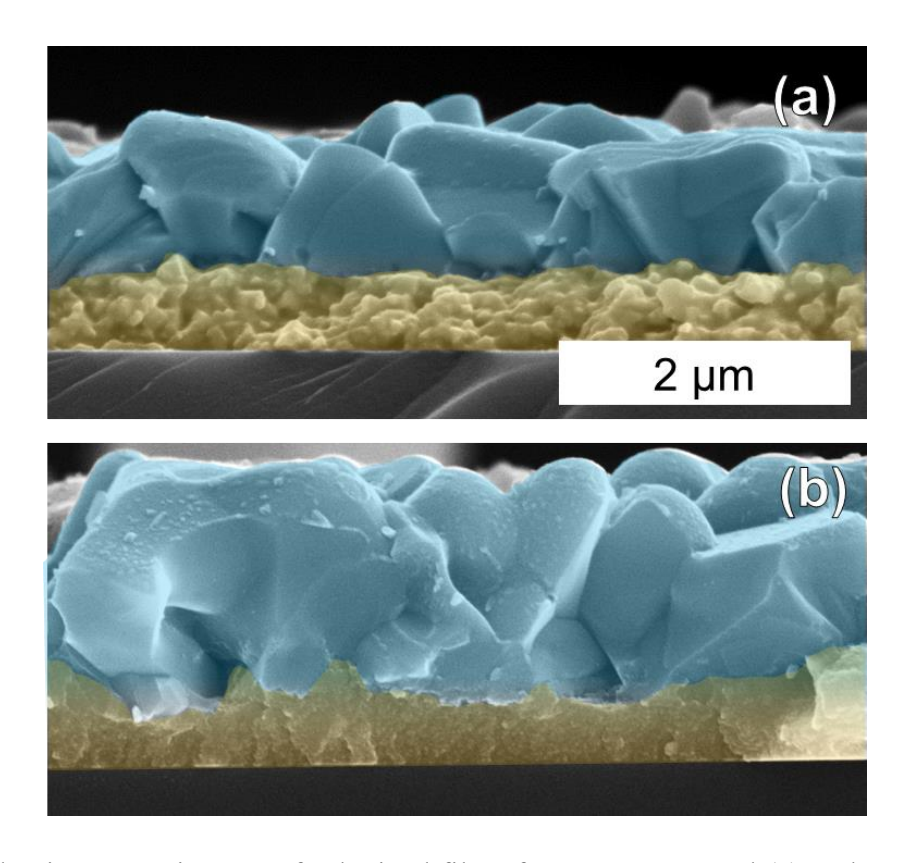


Figure 4. Side view SEM images of selenized films from NMP-capped (a) and OLA-capped (b) nanoparticles. Clearly distinguishable is the bilayer structure with coarse grains (highlighted in blue) on top of a fine grain layer (highlighted in orange) on the bottom in each film. Notable is the fine grain layer in (a) which seems to show enhanced grain growth than that of the more traditionally prepared colloidal nanoparticle film in (b). Scale bar applies to both images.

To check for any potential differences in the fine-grain layer, we first probed the film via Raman spectroscopy. Raman spectroscopy is usually only capable of probing surface-level characteristics at a depth dependent on the wavelength of the excitation laser. For a coarsened sulfide-to-selenide film, a 633 nm excitation laser will be fully absorbed within the first ~200-300 nm of the film and, as a result, only probe the coarse grains in the film, thus not providing any information about the fine-grain layer at the back of the film. To confirm this, we see the Raman spectra from the top surface of two representative films—fabricated from nanoparticles synthesized using OLA or

NMP—appearing nearly identical. Further analysis of the Raman spectra of the top surface of NMP-prepared films suggests the formation of the ordered-vacancy compound with a small shoulder off the left side of the main A1 peak (see **Figure S6**).

In order to overcome this obstacle and to characterize the fine-grain layer via Raman spectroscopy, a quick-cure, two-part epoxy resin was used for a liftoff technique to exfoliate the back surface of the film so that analyses of the fine-grain layers were possible (see Figure 5a for a schematic). Figure 5b shows the resulting Raman spectroscopy of the fine-grain layers from both of the selenized OLA and NMP nanoparticle films. Two significant differences can quickly be seen with the presence of a substantial Se resonance centered at ~252 cm⁻¹ for the OLA spectra as well as the substantial difference of the response for the C-C stretch between ~1200-1700 cm⁻¹ ¹, where even the D and G bands can easily be distinguished at ~1370 and ~1545 cm⁻¹, respectively, for the OLA film. One measure we used to quantify the material quality of the fine-grain layer was to calculate the ratio between the A1 and carbon peaks by using peak area. The A1 peak is the most prominent for typical chalcopyrite crystals and measures the vibrational frequency of the Se atoms against the metal atoms at rest.⁶⁴ Performing this back-of-the-envelope calculation gives us a substantially higher carbon-to-A1 ratio for the OLA film than in the NMP film showing that the NMP film has substantially less carbon than the OLA film in the fine-grain layer. The likely reason for the increased carbon signal is revealed by infrared spectroscopy data (shown in Figure S7) of coated films of each type of nanoparticle, showing significantly higher organic signal from the OLA-capped nanoparticles. This indicates a higher carbon content in the OLA-capped film before selenization. These results, in tandem with the lack of a significant Se response in the NMP finegrain layer, suggests that the quality of the fine-grain layer for the NMP film is much improved over that of the OLA film. This implies that in addition to the high-crystallinity, coarse grains at

the top surface of the film, the fine-grains at the back of the NMP film are also primarily chalcopyrite material.

While visual inspection of the liftoff samples appeared to show a clean liftoff of the entire film, care was taken to double check this. In addition to the Raman measurements taken as depicted in **Figure 5**, Raman measurements were also performed on the location of the original substrate where the liftoff procedure was performed which should ensure that only the fine-grain layer is being probed. This data is shown in **Figure S8**. Here, we see similar results from the film residues as is shown in **Figure 5b**, but more notably, we see the complete lack of any chalcopyrite A1 signal in the OLA-prepared film. More details are provided in the Supplementary Information.

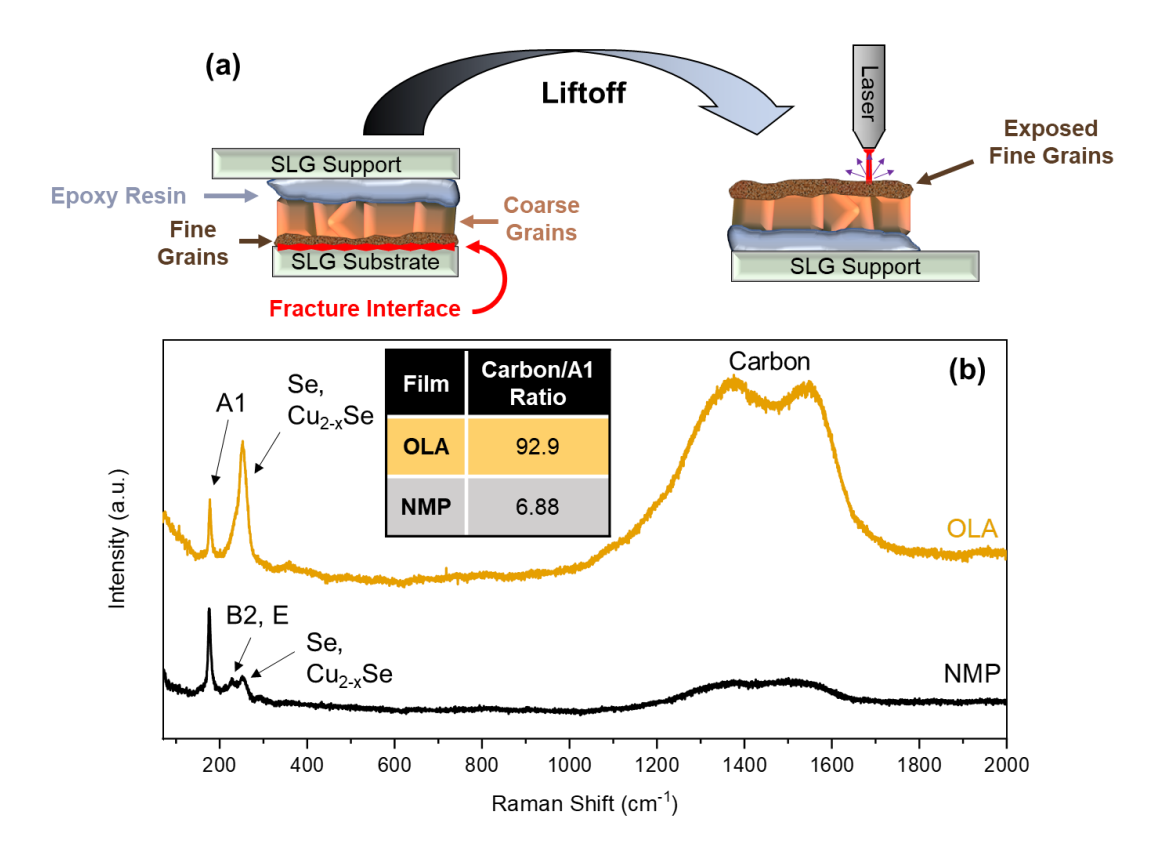


Figure 5. Illustration showing how the epoxy-liftoff procedure is used to exfoliate the film and expose the fine grain layer in (a). Raman spectroscopy of the fine-grain layer from nanoparticle

films from OLA- and NMP-capped nanoparticles in gold and black respectively (b). Table inset in (b) displays the ratio of the integrated areas of the carbon peak to the A1 peak.

In addition to probing the fine-grain layer via Raman spectroscopy, we also performed elemental analysis of the NMP-capped film via STEM-EDX. Shown in Figure 6 is elemental analysis of the fine grain region which presents a few notable differences from traditionally prepared films (see Figure 4b). One prominent difference is the presence of In in the fine-grain layer (see Figure S9). In traditionally prepared films, like the OLA-capped nanoparticle route, the fine grain layer is typically devoid of In (and Ga), and is rich in Cu, C, and Se. The presence of In in the film prepared via the NMP route suggests that grains of CuInSe₂ may exist, which may contribute to carrier generation in devices. Another difference is the observation that the relative carbon content between the coarse-grain and fine-grain layer is nearly identical, likely a result of the volatile ligand species being used, leaving behind minimal carbon residues in the selenized films. Additionally, while it is observed that Cu-rich regions still exist in the fine-grain layer, they form a sort of vascular system which only comprises of a small portion of the total fine-grain layer, thus leaving a substantial portion of the fine-grain layer as Cu-In-Se material. To adequately check our suspicion that the chalcopyrite phase exists in the fine-grain layer, a selected-area electron diffraction measurement, shown in Figure S10, was performed and reveals the main diffractions from CuInSe₂ crystallites, which are distinguished in the figure, indicating the presence of chalcopyrite CuInSe₂ in the fine-grain layer of these films. Additional STEM-EDX characterization is shown in Figures S11-S12 which show the full film and a higher-resolution view of a Cu-rich vein.

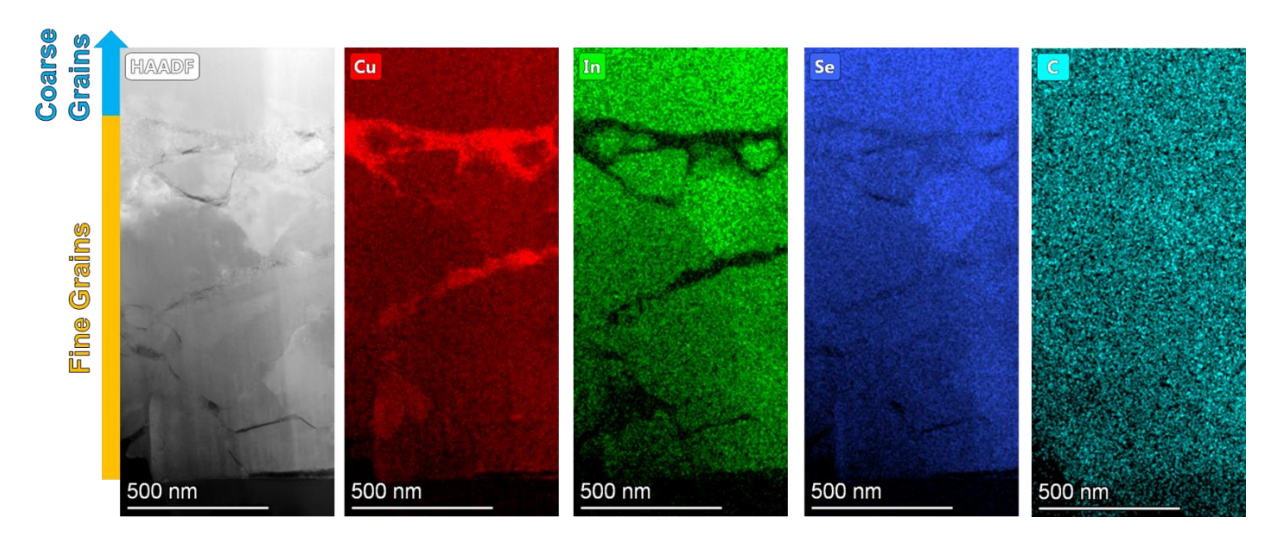


Figure 6. STEM-EDX of a selenized NMP-capped nanoparticle film. Shown are the HAADF, Cu, In, Se, and C intensity maps. Notable are the veins in the fine-grain layer that are rich in Cu and poor in In. The C map is presented to show the reader that no relative changes are observed in the C content between the coarse and fine grain regions. Although special care was taken, the reader is reminded that carbon deposition from dust and other organic particulates in ambient air during sample transport is a potential source of contamination. Additionally, carbon can often be deposited as a contaminant during electron microscopy measurements, Thus, the C map should only be interpreted through relative changes in intensity between regions. S maps are not shown since characterization was performed on Mo sample grids. Mo L-lines overlap strongly with S K-lines, making elemental analysis with the two elements present together unreliable.

Device Characterization

Devices were fabricated following the traditional device stack of Mo/CISSe/CdS/ZnO/ITO with Ag grids followed by MgF₂ deposition on selected samples to act as an anti-reflective coating to increase light-collection capabilities. An SEM image of a completed device cross-section is shown in **Figure S13**. J-V measurements were taken under standard AM1.5 illumination conditions. J-V

data for all devices used in this study is shown in **Figure S14**, but the results for the champion CISSe device is shown in **Figure 7** with all device parameters summarized in **Table 1**. We remind the reader that gallium-containing devices were not measured in this work due to difficulties in creating a homogeneous ink of CIGS nanoparticles, thus leading to difficulties in producing a quality film. To understand the relative performance of our champion device, we compared its device parameters with the respective Detailed Balance limits based on its bandgap energy. Using the bandgap estimation from EQE (**Figure 7b**) of 1.02 eV, we used 47.1 mA/cm², 782 mV, 85.8%, and 31.6% as the Detailed Balance limits for short-circuit current density (J_{SC}), open-circuit voltage (V_{OC}), fill factor (FF), and efficiency (η), respectively. Upon determining the normalized device parameters (also shown in **Table 1**) we see that the J_{SC} stands out for the CISSe champion device. Being 88% of the Detailed Balance limit, this device is among the highest for short-circuit current densities reported so far for a solution-processed device in the CIGSSe family. 3.66

Table 1. Device parameters determined from J-V analysis of the champion device.^a

	J _{SC} (mA/cm ²)	Voc (mV)	FF (%)	η (%)	$R_{s,light}$ $(\Omega \text{ cm}^2)$	$R_{sh,light}$ $(\Omega \text{ cm}^2)$	n,light	J _{0,light} (mA/cm ²)
Measured	41.6 (36.1)	455 (435)	58.5 (54.7)	11.1 (8.6)	1.02	247	2.1	7.07×10 ⁻³
% Limit	88.3 (76.6)	58.2 (55.6)	68.2 (63.8)	35.1 (27.2)	-	-	-	-

^aActive area was used to calculate short-circuit current density and total efficiency. Average device values are shown in parenthesis. R_s, R_{sh}, diode ideality factor, n, and the diode saturation current, J₀ were determined using the diode equation for solar cells. Further discussion on derivation is provided in the Supplementary Information.

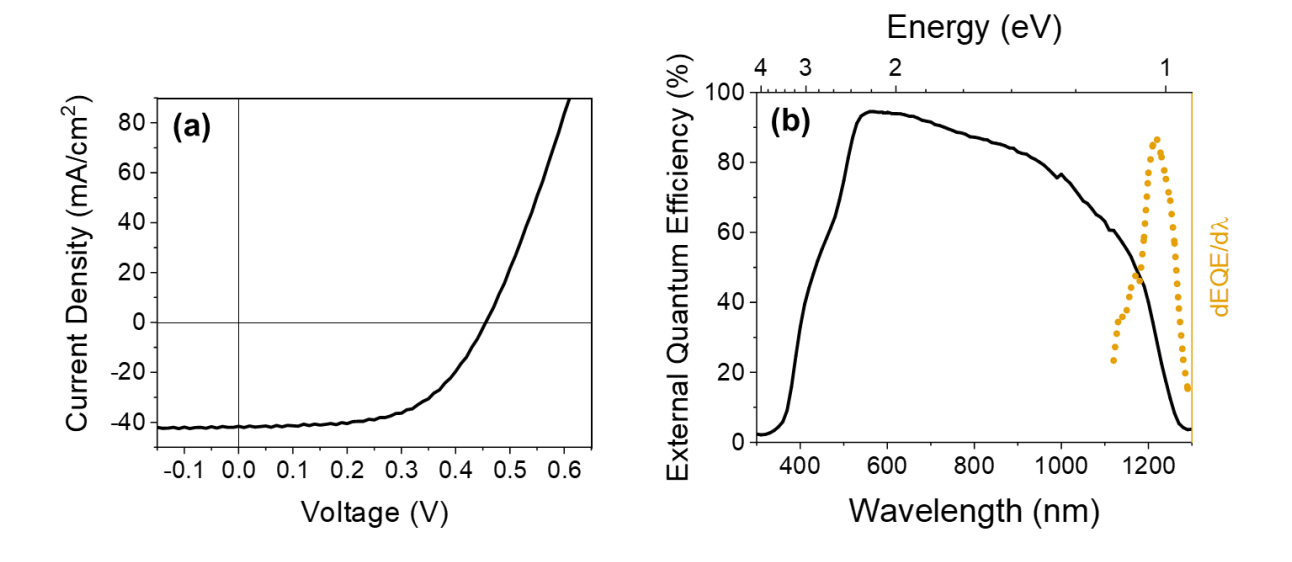


Figure 7. (a) J-V curve of the champion CISSe device. (b) EQE of the champion CISSe device with estimated bandgap using the derivative method. The non-zero readings at the two extremes of (b) are artifacts from transforming the raw data using calibrated measurements. Further explanation is given in the Supplementary Information.

With this particular device, we can see that there are still fairly substantial losses related to opencircuit voltage (V_{OC}) and fill factor (FF). V_{OC} is essentially a measure of the amount of recombination in a device that may have contributions from the bulk and/or surfaces/interfaces.⁶⁷ Surface/interface recombination, for example, can be mitigated by creating more chemically and electrically benign interfaces between the subsequent layers in a completed device. This can include increasing Cd^{2+} diffusion during CdS deposition into the CIGSSe layer through incorporation of a Cu-deficient layer at the surface of the CIGSSe absorber layer.⁶⁸ In the case of this work, it seems likely that V_{OC} losses are a result of recombination at the CISSe/CdS interface (see **Figure S15**). No Cu-deficient layer nor a heavy-alkali treatment was implemented, both of which are known to promote surface passivation of CISSe grains, resulting in increases to V_{OC} .^{69,70} FF losses are also apparent, indicating losses from increased series resistance (R_s), decreased shunt resistance (R_{sh}), and increased diode ideality factor. Some attributions may be pinholes in the absorber layer leading to increased shunt pathways, and increased recombination in the depletion region, which is typically believed to lead to a higher diode ideality factor.⁷¹

Figure 7b shows the external quantum efficiency (EQE) of the same device taken under "dark" conditions (no external light bias was applied). EQE allows us to understand the absorption capabilities of a device as a function of wavelength, which is useful for bandgap estimation and understanding losses related to carrier generation and collection. To estimate the device's bandgap, the derivative of the EQE response with respect to the wavelength was measured in the high wavelength region of the plot near the material's bandgap. Here we see the inflection point in the EQE response occurs at a wavelength of 1220 nm, corresponding to an average bandgap for this device of 1.02 eV. Further analysis of the EQE response shows a steady drop-off after reaching a maximum of 95% collection at 560 nm to 76% at 1000 nm before dropping off sharply as it approaches the device's bandgap. This downward slope in the collection at higher wavelengths indicates that the device is less efficiently collecting and/or generating carriers deeper in the film.

To determine the potential source of this issue, voltage-dependent EQE was performed and is shown in **Figure S15**. Here, we see virtually no difference between the non-biased EQE signal and the signal at negative biases in the longer wavelength region. If carriers were having trouble reaching the front surface of the device due to low diffusion lengths, increasing the depletion region width with a negatively-applied bias would aid carrier collection. Thus, we attribute the downward slope in the unbiased EQE as a result of incomplete absorption of higher wavelength photons. Resolving this issue could be performed by increasing the thickness of the absorber layer, giving high-wavelength photons a higher probability of exciting carriers near the back of the film.

One thing to note is that a noticeable increase in the ratio of the negatively-biased EQE to the non-biased EQE is seen as the wavelength decreases, beginning almost exactly at the bandgap of CdS (2.42 eV). This implies that the collection gain seen in the -0.4 V bias signal is likely due to improved carrier collection of excited carriers in CdS from these lower-wavelength photons due to more favorable charge collection at the ZnO/CdS interface.⁷² More discussion on the voltage-biased EQE is given in the Supplementary Information section.

The short-circuit current density was also estimated by integrating the EQE curve with the AM1.5G spectra and is shown in **Figure S16**. Upon integration, we find that there is a 4.5 mA/cm² difference between the J_{SC} values obtained from the J-V measurements, 41.6 mA/cm², and that of the EQE curve, 37.1 mA/cm². Some potential reasons for this difference are discussed here. Since only a small portion of the device is illuminated during EQE measurements (~10% of the active area of the device), the non-illuminated parts can act as a shunting load, providing shunt pathways for current loss. Since a moderately low R_{sh} of 247 Ω^* cm² was calculated, it is reasonable to expect some losses for this reason. 73 Additionally, the illuminated region may have been more defective than the remainder of the device, leading to the lower integrated J_{SC,EOE}. Another possible reason for the lower J_{SC,FOE} could be due to the absence of a DC light bias during EQE measurements. The presence of a DC light bias allows for closer imitation of the device properties under normal operating conditions, allowing for the entire device to saturate with carriers and to avoid metastabilities before performing spectral responsivity measurements. It has been shown previously that a light-biased EQE response shows increases in integrated J_{SC} from EQE data over a "dark" EQE response (no light bias)⁷⁴ and is most notable in the region from none to low light biases.⁷⁵

Conclusion:

While further investigations are still needed in the syntheses of gallium-containing CIGS nanoparticles via the NMP/metal chlorides route—for better suspensions, thus allowing for higher quality ink-coated films—the industrially-relevant solvent, NMP, has proven itself to be an effective substitute for the high molecular-weight species, like OLA, typically used as coordinating agents in colloidal nanoparticle syntheses. Additionally, its effectiveness in its use as the coating solvent to produce smooth films further helps to decrease the complexity of this process as a whole by minimizing the overall number of different components to a once complex process. One key takeaway from these results is the improved character of the fine-grain layer of these new films both in its decreased carbon content and increased chalcopyrite content—indicating that highquality grains exist throughout the film regardless of their size, leading to a film with more homogeneous optoelectronic properties throughout, all while bypassing the complex ligandexchange process. This is likely the reason for the high short-circuit current density of 41.6 mA/cm², as the entire device can generate carriers in a similar fashion. Improvements to film fabrication and optimization of the remaining buffer and window layers should help further improve device performances by decreasing losses to both V_{OC} and FF. Ultimately, the use of NMP and other volatile species as a crucial ingredient for the fabrication of high-quality, lowcarbon CIGSSe solar cells is promising.

Associated Content

Supporting Information

The following files are available free of charge.

Additional pXRD data, TEM images, experimental considerations during nanoparticle syntheses, additional Raman spectra, FTIR spectroscopy data, SAED data, STEM-EDX data, SEM images, and device data. (PDF)

Author Information

Corresponding Authors

Rakesh Agrawal – Davidson School of Chemical Engineering, Purdue University, West Lafayette, IN, USA; orcid.org/0000-0002-6746-9829;

Email: agrawalr@purdue.edu

Authors

Daniel C. Hayes – Davidson School of Chemical Engineering, Purdue University, West Lafayette, IN, USA; orcid.org/0009-0006-3953-6373

Samantha A. Langdon – Davidson School of Chemical Engineering, Purdue University, West Lafayette, IN, USA

Robert M. Spilker – Davidson School of Chemical Engineering, Purdue University, West Lafayette, IN, USA; orcid.org/0009-0005-7079-6125

Notes

The authors declare no competing financial interest.

Acknowledgements

The authors are grateful for the financial support from the National Science Foundation through grants 1735282-NRT (SFEWS) and 10001536 (INFEWS). We are also thankful to Jonathan Turnley for collecting ¹H NMR data and for assistance in providing Mo-coated soda-lime glass substrates and for general guidance throughout the preparation of this manuscript. We would also like to thank Apurva Pradhan and Shubhanshu Agarwal for their comments and suggestions during the revision process of this manuscript and would additionally like to thank Ryan Ellis and David Rokke for their guidance early in the experimental phases of this project.

References:

- (1) Nakamura, M.; Yamaguchi, K.; Kimoto, Y.; Yasaki, Y.; Kato, T.; Sugimoto, H. Cd-Free Cu(In,Ga)(Se,S) 2 Thin-Film Solar Cell With Record Efficiency of 23.35%. *IEEE J Photovolt* **2019**, *9* (6), 1863–1867. https://doi.org/10.1109/JPHOTOV.2019.2937218.
- (2) NREL. Best Research-Cell Efficiencies; 2023. https://www.nrel.gov/pv/cell-efficiency.html.
- (3) Suresh, S.; Uhl, A. R. Present Status of Solution-Processing Routes for Cu(In,Ga)(S,Se) 2 Solar Cell Absorbers. *Adv Energy Mater* **2021**, *11* (14), 2003743. https://doi.org/10.1002/aenm.202003743.
- Wu, S.; Jiang, J.; Yu, S.; Gong, Y.; Yan, W.; Xin, H.; Huang, W. Over 12% Efficient Low-Bandgap CuIn(S, Se)2 Solar Cells with the Absorber Processed from Aqueous Metal Complexes Solution in Air. *Nano Energy* **2019**, *62* (April), 818–822. https://doi.org/10.1016/j.nanoen.2019.06.010.
- (5) Hossain, Md. A.; Tianliang, Z.; Keat, L. K.; Xianglin, L.; Prabhakar, R. R.; Batabyal, S. K.; Mhaisalkar, S. G.; Wong, L. H. Synthesis of Cu(In,Ga)(S,Se) 2 Thin Films Using an Aqueous Spray-Pyrolysis Approach, and Their Solar Cell Efficiency of 10.5%. *J Mater Chem A Mater* **2015**, *3* (8), 4147–4154. https://doi.org/10.1039/C4TA05783J.
- (6) Kim, S.; Mina, Md. S.; Lee, J.; Kim, J. Sulfur-Alloying Effects on Cu(In,Ga)(S,Se) 2 Solar Cell Fabricated Using Aqueous Spray Pyrolysis. *ACS Appl Mater Interfaces* **2019**, *11* (49), 45702–45708. https://doi.org/10.1021/acsami.9b16192.
- (7) Uhl, A. R.; Romanyuk, Y. E.; Tiwari, A. N. Thin Film Cu(In,Ga)Se2 Solar Cells Processed from Solution Pastes with Polymethyl Methacrylate Binder. *Thin Solid Films* **2011**, *519* (21), 7259–7263. https://doi.org/10.1016/j.tsf.2011.01.136.
- (8) Park, G. S.; Chu, V. Ben; Kim, B. W.; Kim, D.-W.; Oh, H.-S.; Hwang, Y. J.; Min, B. K. Achieving 14.4% Alcohol-Based Solution-Processed Cu(In,Ga)(S,Se) 2 Thin Film Solar Cell through Interface Engineering. *ACS Appl Mater Interfaces* **2018**, *10* (12), 9894–9899. https://doi.org/10.1021/acsami.8b00526.
- (9) Mitzi, D. B.; Yuan, M.; Liu, W.; Kellock, A. J.; Chey, S. J.; Deline, V.; Schrott, A. G. A High-Efficiency Solution-Deposited Thin-Film Photovoltaic Device. *Advanced Materials* **2008**, *20* (19), 3657–3662. https://doi.org/10.1002/adma.200800555.
- (10) Todorov, T. K.; Gunawan, O.; Gokmen, T.; Mitzi, D. B. Solution-Processed Cu(In,Ga)(S,Se) 2 Absorber Yielding a 15.2% Efficient Solar Cell. **2012**. https://doi.org/10.1002/pip.1253.
- (11) Zhang, T.; Yang, Y.; Liu, D.; Tse, S. C.; Cao, W.; Feng, Z.; Chen, S.; Qian, L. High Efficiency Solution-Processed Thin-Film Cu(In,Ga)(Se,S) 2 Solar Cells. *Energy Environ Sci* **2016**, *9* (12), 3674–3681. https://doi.org/10.1039/C6EE02352E.

- (12) Zhao, X.; Lu, M.; Koeper, M. J.; Agrawal, R. Solution-Processed Sulfur Depleted Cu(In, Ga)Se 2 Solar Cells Synthesized from a Monoamine–Dithiol Solvent Mixture. *J Mater Chem A Mater* **2016**, *4* (19), 7390–7397. https://doi.org/10.1039/C6TA00533K.
- (13) Deshmukh, S. D.; Weideman, K. G.; Ellis, R. G.; Kisslinger, K.; Agrawal, R. Enabling Fine-Grain Free 2-Micron Thick CISe/CIGSe Film Fabrication via a Non-Hydrazine Based Solution Processing Route. *Mater Adv* **2022**, *3* (7), 3293–3302. https://doi.org/10.1039/D2MA00095D.
- (14) Zhao, Y.; Yuan, S.; Chang, Q.; Zhou, Z.; Kou, D.; Zhou, W.; Qi, Y.; Wu, S. Controllable Formation of Ordered Vacancy Compound for High Efficiency Solution Processed Cu(In,Ga)Se 2 Solar Cells. *Adv Funct Mater* **2021**, *31* (10), 2007928. https://doi.org/10.1002/adfm.202007928.
- (15) Panthani, M. G.; Akhavan, V.; Goodfellow, B.; Schmidtke, J. P.; Dunn, L.; Dodabalapur, A.; Barbara, P. F.; Korgel, B. A. Synthesis of CuInS 2, CuInSe 2, and Cu(In x Ga 1- x)Se 2 (CIGS) Nanocrystal "Inks" for Printable Photovoltaics. *J Am Chem Soc* **2008**, *130* (49), 16770–16777. https://doi.org/10.1021/ja805845q.
- (16) Jeong, S.; Lee, B.-S.; Ahn, S.; Yoon, K.; Seo, Y.-H.; Choi, Y.; Ryu, B.-H. An 8.2% Efficient Solution-Processed CuInSe2 Solar Cell Based on Multiphase CuInSe2 Nanoparticles. *Energy Environ Sci* **2012**, *5* (6), 7539. https://doi.org/10.1039/c2ee21269b.
- (17) Ellis, R. G.; Turnley, J. W.; Rokke, D. J.; Fields, J. P.; Alruqobah, E. H.; Deshmukh, S. D.; Kisslinger, K.; Agrawal, R. Hybrid Ligand Exchange of Cu(In,Ga)S 2 Nanoparticles for Carbon Impurity Removal in Solution-Processed Photovoltaics. *Chemistry of Materials* **2020**, *32* (12), 5091–5103. https://doi.org/10.1021/acs.chemmater.0c00966.
- (18) McLeod, S. M.; Hages, C. J.; Carter, N. J.; Agrawal, R. Synthesis and Characterization of 15% Efficient CIGSSe Solar Cells from Nanoparticle Inks. *Progress in Photovoltaics: Research and Applications* **2015**, *23* (11), 1550–1556. https://doi.org/10.1002/pip.2588.
- (19) Boles, M. A.; Ling, D.; Hyeon, T.; Talapin, D. V. The Surface Science of Nanocrystals. *Nat Mater* **2016**, *15* (2), 141–153. https://doi.org/10.1038/nmat4526.
- (20) Guo, Q.; Kim, S. J.; Kar, M.; Shafarman, W. N.; Birkmire, R. W.; Stach, E. A.; Agrawal, R.; Hillhouse, H. W. Development of CuInSe 2 Nanocrystal and Nanoring Inks for Low-Cost Solar Cells. *Nano Lett* **2008**, *8* (9), 2982–2987. https://doi.org/10.1021/nl802042g.
- (21) Marin, R.; Skripka, A.; Huang, Y.-C.; Loh, T. A. J.; Mazeika, V.; Karabanovas, V.; Chua, D. H. C.; Dong, C.-L.; Canton, P.; Vetrone, F. Influence of Halide Ions on the Structure and Properties of Copper Indium Sulphide Quantum Dots. *Chemical Communications* **2020**, *56* (22), 3341–3344. https://doi.org/10.1039/C9CC08291C.
- (22) Ellis, R. G.; Deshmukh, S. D.; Turnley, J. W.; Sutandar, D. S.; Fields, J. P.; Agrawal, R. Direct Synthesis of Sulfide-Capped Nanoparticles for Carbon-Free Solution-Processed Photovoltaics. *ACS Appl Nano Mater* **2021**, *4* (11), 11466–11472. https://doi.org/10.1021/acsanm.1c02561.

- (23) Dolzhnikov, D. S.; Zhang, H.; Jang, J.; Son, J. S.; Panthani, M. G.; Shibata, T.; Chattopadhyay, S.; Talapin, D. V. Composition-Matched Molecular "Solders" for Semiconductors. *Science* (1979) **2015**, 347 (6220), 425–428. https://doi.org/10.1126/science.1260501.
- (24) Dierick, R.; Capon, B.; Damm, H.; Flamee, S.; Arickx, P.; Bruneel, E.; Van Genechten, D.; Van Bael, M.; Hardy, A.; Detavernier, C.; Hens, Z. Annealing of Sulfide Stabilized Colloidal Semiconductor Nanocrystals. *J. Mater. Chem. C* **2014**, *2* (1), 178–183. https://doi.org/10.1039/C3TC31393J.
- (25) Nag, A.; Kovalenko, M. V.; Lee, J. S.; Liu, W.; Spokoyny, B.; Talapin, D. V. Metal-Free Inorganic Ligands for Colloidal Nanocrystals: S2-, HS-, Se2-, HSe-, Te2-, HTe-, TeS32-, OH-, and NH 2- as Surface Ligands. *J Am Chem Soc* 2011, 133 (27), 10612–10620. https://doi.org/10.1021/ja2029415.
- (26) Coughlan, C.; Ibáñez, M.; Dobrozhan, O.; Singh, A.; Cabot, A.; Ryan, K. M. Compound Copper Chalcogenide Nanocrystals. *Chem Rev* **2017**, *117* (9), 5865–6109. https://doi.org/10.1021/acs.chemrev.6b00376.
- (27) McLeod, S.; Alruqobah, E.; Agrawal, R. Liquid Assisted Grain Growth in Solution Processed Cu(In,Ga)(S,Se)2. *Solar Energy Materials and Solar Cells* **2019**, *195*, 12–23. https://doi.org/10.1016/j.solmat.2019.02.020.
- (28) Hages, C. J.; Koeper, M. J.; Miskin, C. K.; Brew, K. W.; Agrawal, R. Controlled Grain Growth for High Performance Nanoparticle-Based Kesterite Solar Cells. *Chemistry of Materials* **2016**, *28* (21), 7703–7714. https://doi.org/10.1021/acs.chemmater.6b02733.
- (29) Rehan, S.; Kim, K. Y.; Han, J.; Eo, Y.-J.; Gwak, J.; Ahn, S. K.; Yun, J. H.; Yoon, K.; Cho, A.; Ahn, S. Carbon-Impurity Affected Depth Elemental Distribution in Solution-Processed Inorganic Thin Films for Solar Cell Application. *ACS Appl Mater Interfaces* **2016**, *8* (8), 5261–5272. https://doi.org/10.1021/acsami.5b10789.
- (30) Zhao, D.; Fan, Q.; Tian, Q.; Zhou, Z.; Meng, Y.; Kou, D.; Zhou, W.; Wu, S. Eliminating Fine-Grained Layers in Cu(In,Ga)(S,Se) 2 Thin Films for Solution-Processed High Efficiency Solar Cells. *J Mater Chem A Mater* **2016**, *4* (35), 13476–13481. https://doi.org/10.1039/C6TA05728D.
- (31) Xin, H.; Katahara, J. K.; Braly, I. L.; Hillhouse, H. W. 8% Efficient Cu 2 ZnSn(S,Se) 4 Solar Cells from Redox Equilibrated Simple Precursors in DMSO. *Adv Energy Mater* **2014**, 4 (11), 1301823. https://doi.org/10.1002/aenm.201301823.
- (32) Martin, T. R.; Katahara, J. K.; Bucherl, C. N.; Krueger, B. W.; Hillhouse, H. W.; Luscombe, C. K. Nanoparticle Ligands and Pyrolized Graphitic Carbon in CZTSSe Photovoltaic Devices. *Chemistry of Materials* **2016**, *28* (1), 135–145. https://doi.org/10.1021/acs.chemmater.5b03426.
- (33) NREL. Best Research-Cell Efficiencies; 2022. https://www.nrel.gov/pv/cell-efficiency.html.

- (34) Korala, L.; Braun, M. B.; Kephart, J. M.; Tregillus, Z.; Prieto, A. L. Ligand-Exchanged CZTS Nanocrystal Thin Films: Does Nanocrystal Surface Passivation Effectively Improve Photovoltaic Performance? *Chemistry of Materials* **2017**, *29* (16), 6621–6629. https://doi.org/10.1021/acs.chemmater.7b00541.
- (35) Eeles, A.; Arnou, P.; Bowers, J. W.; Walls, J. M.; Whitelegg, S.; Kirkham, P.; Allen, C.; Stubbs, S.; Liu, Z.; Masala, O.; Newman, C.; Pickett, N. High-Efficiency Nanoparticle Solution-Processed Cu(In,Ga)(S,Se)2 Solar Cells. *IEEE J Photovolt* **2018**, *8* (1), 288–292. https://doi.org/10.1109/JPHOTOV.2017.2762581.
- (36) Ritchie, C.; Chesman, A. S. R.; Jasieniak, J.; Mulvaney, P. Aqueous Synthesis of Cu 2 ZnSnSe 4 Nanocrystals. *Chemistry of Materials* **2019**, *31* (6), 2138–2150. https://doi.org/10.1021/ACS.CHEMMATER.9B00100/SUPPL_FILE/CM9B00100_SI_00 1.PDF.
- (37) Lee, J. H.; Chang, J.; Cha, J.; Lee, Y.; Han, J. E.; Jung, D.; Choi, E. C.; Hong, B. Large-Scale, Surfactant-Free Solution Syntheses of Cu(In,Ga)(S,Se) 2 Nanocrystals for Thin Film Solar Cells. *Eur J Inorg Chem* **2011**, *2011* (5), 647–651. https://doi.org/10.1002/ejic.201000967.
- (38) Badgujar, A. C.; Dusane, R. O.; Dhage, S. R. Sonochemical Synthesis of CuIn0.7Ga0.3Se2 Nanoparticles for Thin Film Photo Absorber Application. *Mater Sci Semicond Process* **2018**, *81* (February), 17–21. https://doi.org/10.1016/j.mssp.2018.03.001.
- (39) Thi, T.; Le, T.; Le, N.; Reddy Pallavolu, M.; Jeon, Y.; Jeong, D.-S.; Pejjai, B.; Reddy, V.; Reddy, M.; Tam, N.; Truong, N.; Park, C. Green and Low-Cost Preparation of CIGSe Thin Film by a Nanocrystals Ink Based Spin-Coating Method. *Korean J. Chem. Eng* **2019**, *36* (12), 2110–2117. https://doi.org/10.1007/s11814-019-0386-8.
- (40) Cha, J.; Noh, S. J.; Jung, D. Synthesis and Nanostructures of Metal Selenide Precursors for Cu(In,Ga)Se 2 Thin-Film Solar Cells. *ChemSusChem* **2015**, 8 (14), 2407–2413. https://doi.org/10.1002/cssc.201403464.
- (41) Wu, C.; Wang, D.; Zhang, Y.; Gu, F.; Liu, G.; Zhu, N.; Luo, W.; Han, D.; Guo, X.; Qu, B.; Wang, S.; Bian, Z.; Chen, Z.; Xiao, L. FAPbI 3 Flexible Solar Cells with a Record Efficiency of 19.38% Fabricated in Air via Ligand and Additive Synergetic Process. *Adv Funct Mater* **2019**, *29* (34), 1902974. https://doi.org/10.1002/adfm.201902974.
- (42) Muñoz, S. B.; Daifuku, S. L.; Sears, J. D.; Baker, T. M.; Carpenter, S. H.; Brennessel, W. W.; Neidig, M. L. The N -Methylpyrrolidone (NMP) Effect in Iron-Catalyzed Cross-Coupling with Simple Ferric Salts and MeMgBr. *Angewandte Chemie International Edition* **2018**, *57* (22), 6496–6500. https://doi.org/10.1002/anie.201802087.
- (43) Churchill, M. R.; Rotella, F. J. Crystal Structure and Molecular Configuration of a Tetranuclear Copper(II) Complex Active as a Catalyst in the Oxidative Coupling of Phenols by Dioxygen: Cu4OCl6(Nmp)3(OH2.Cntdot..Cntdot..Cntdot.Nmp) (Nmp = N-Methyl-2-Pyrrolidinone). *Inorg Chem* **1979**, *18* (3), 853–860. https://doi.org/10.1021/ic50193a063.

- (44) Ding, K.; Zannat, F.; Morris, J. C.; Brennessel, W. W.; Holland, P. L. Coordination of N-Methylpyrrolidone to Iron(II). *J Organomet Chem* **2009**, *694* (26), 4204–4208. https://doi.org/10.1016/j.jorganchem.2009.09.005.
- (45) Zhang, X.; Lai, Z.; Liu, Z.; Tan, C.; Huang, Y.; Li, B.; Zhao, M.; Xie, L.; Huang, W.; Zhang, H. A Facile and Universal Top-Down Method for Preparation of Monodisperse Transition-Metal Dichalcogenide Nanodots. *Angewandte Chemie* **2015**, *127* (18), 5515–5518. https://doi.org/10.1002/ange.201501071.
- (46) Coleman, J. N.; Lotya, M.; O'Neill, A.; Bergin, S. D.; King, P. J.; Khan, U.; Young, K.; Gaucher, A.; De, S.; Smith, R. J.; Shvets, I. V.; Arora, S. K.; Stanton, G.; Kim, H.-Y.; Lee, K.; Kim, G. T.; Duesberg, G. S.; Hallam, T.; Boland, J. J.; Wang, J. J.; Donegan, J. F.; Grunlan, J. C.; Moriarty, G.; Shmeliov, A.; Nicholls, R. J.; Perkins, J. M.; Grieveson, E. M.; Theuwissen, K.; McComb, D. W.; Nellist, P. D.; Nicolosi, V. Two-Dimensional Nanosheets Produced by Liquid Exfoliation of Layered Materials. *Science* (1979) 2011, 331 (6017), 568–571. https://doi.org/10.1126/science.1194975.
- (47) Ravi, V. K.; Yu, S. H.; Rajput, P. K.; Nayak, C.; Bhattacharyya, D.; Chung, D. S.; Nag, A. Colloidal BaZrS 3 Chalcogenide Perovskite Nanocrystals for Thin Film Device Fabrication. *Nanoscale* **2021**, *13* (3), 1616–1623. https://doi.org/10.1039/D0NR08078K.
- (48) Rezaee, E.; Kutsarov, D.; Li, B.; Bi, J.; Silva, S. R. P. A Route towards the Fabrication of Large-Scale and High-Quality Perovskite Films for Optoelectronic Devices. *Sci Rep* **2022**, *12* (1), 7411. https://doi.org/10.1038/s41598-022-10790-z.
- (49) Li, Z.; Li, P.; Chen, G.; Cheng, Y.; Pi, X.; Yu, X.; Yang, D.; Han, L.; Zhang, Y.; Song, Y. Ink Engineering of Inkjet Printing Perovskite. *ACS Appl Mater Interfaces* **2020**, *12* (35), 39082–39091. https://doi.org/10.1021/acsami.0c09485.
- (50) Jouyban, A.; Fakhree, M. A. A.; Shayanfar, A. Review of Pharmaceutical Applications of N-Methyl-2-Pyrrolidone. *Journal of Pharmacy & Pharmaceutical Sciences* 2010, 13 (4), 524. https://doi.org/10.18433/J3P306.
- (51) Porzio, J.; Scown, C. D. Life-Cycle Assessment Considerations for Batteries and Battery Materials. *Adv Energy Mater* **2021**, *11* (33), 2100771. https://doi.org/10.1002/aenm.202100771.
- (52) He, R.; Qian, X.; Yin, J.; Zhu, Z. Preparation of Polychrome Silver Nanoparticles in Different Solvents. *J Mater Chem* **2002**, *12* (12), 3783–3786. https://doi.org/10.1039/b205214h.
- (53) Koskela, K. M.; Strumolo, M. J.; Brutchey, R. L. Progress of Thiol-Amine 'Alkahest' Solutions for Thin Film Deposition. *Trends Chem* **2021**, *3* (12), 1061–1073. https://doi.org/10.1016/j.trechm.2021.09.006.
- (54) Scheer, R.; Schock, H. Thin Film Material Properties. In *Chalcogenide Photovoltaics*; Wiley, 2011; pp 175–234. https://doi.org/10.1002/9783527633708.ch4.

- (55) Deshmukh, S. D.; Ellis, R. G.; Sutandar, D. S.; Rokke, D. J.; Agrawal, R. Versatile Colloidal Syntheses of Metal Chalcogenide Nanoparticles from Elemental Precursors Using Amine-Thiol Chemistry. *Chemistry of Materials* **2019**, *31* (21), 9087–9097. https://doi.org/10.1021/acs.chemmater.9b03401.
- (56) Tappan, B. A.; Barim, G.; Kwok, J. C.; Brutchey, R. L. Utilizing Diselenide Precursors toward Rationally Controlled Synthesis of Metastable CuInSe 2 Nanocrystals. *Chemistry of Materials* **2018**, *30* (16), 5704–5713. https://doi.org/10.1021/acs.chemmater.8b02205.
- (57) Thomson, J. W.; Nagashima, K.; Macdonald, P. M.; Ozin, G. A. From Sulfur–Amine Solutions to Metal Sulfide Nanocrystals: Peering into the Oleylamine–Sulfur Black Box. *J Am Chem Soc* **2011**, *133* (13), 5036–5041. https://doi.org/10.1021/JA1109997.
- (58) De Roo, J.; Yazdani, N.; Drijvers, E.; Lauria, A.; Maes, J.; Owen, J. S.; Driessche, I. Van; Niederberger, M.; Wood, V.; Martins, J. C.; Infante, I.; Hens, Z. Probing Solvent–Ligand Interactions in Colloidal Nanocrystals by the NMR Line Broadening. **2018**. https://doi.org/10.1021/acs.chemmater.8b02523.
- (59) Dierick, R.; Van den Broeck, F.; De Nolf, K.; Zhao, Q.; Vantomme, A.; Martins, J. C.; Hens, Z. Surface Chemistry of CuInS 2 Colloidal Nanocrystals, Tight Binding of L-Type Ligands. *Chemistry of Materials* **2014**, *26* (20), 5950–5957. https://doi.org/10.1021/cm502687p.
- (60) Lemus-Santana, A. A.; González, M.; Rodríguez-Hernández, J.; Knobel, M.; Reguera, E. 1-Methyl-2-Pyrrolidone: From Exfoliating Solvent to a Paramagnetic Ligand. *Journal of Physical Chemistry A* **2013**, *117* (11), 2400–2407. https://doi.org/10.1021/JP4007813.
- (61) Guo, Q.; Ford, G. M.; Agrawal, R.; Hillhouse, H. W. Ink Formulation and Low-Temperature Incorporation of Sodium to Yield 12% Efficient Cu(In,Ga)(S,Se) 2 Solar Cells from Sulfide Nanocrystal Inks. *Progress in Photovoltaics: Research and Applications* **2013**, 21 (1), 64–71. https://doi.org/10.1002/pip.2200.
- (62) Miskin, C. K.; Yang, W.-C.; Hages, C. J.; Carter, N. J.; Joglekar, C. S.; Stach, E. A.; Agrawal, R. 9.0% Efficient Cu 2 ZnSn(S,Se) 4 Solar Cells from Selenized Nanoparticle Inks. *Progress in Photovoltaics: Research and Applications* **2015**, *23* (5), 654–659. https://doi.org/10.1002/pip.2472.
- (63) Suresh, S.; Rokke, D. J.; Drew, A. A.; Alruqobah, E.; Agrawal, R.; Uhl, A. R. Extrinsic Doping of Ink-Based Cu(In,Ga)(S,Se)2-Absorbers for Photovoltaic Applications. *Adv Energy Mater* **2022**, *12* (18), 1–34. https://doi.org/10.1002/aenm.202103961.
- (64) Rincón, C.; Ramírez, F. J. Lattice Vibrations of CuInSe 2 and CuGaSe 2 by Raman Microspectrometry. *J Appl Phys* **1992**, 72 (9), 4321–4324. https://doi.org/10.1063/1.352195.
- (65) Krückemeier, L.; Rau, U.; Stolterfoht, M.; Kirchartz, T. How to Report Record Open-Circuit Voltages in Lead-Halide Perovskite Solar Cells. *Adv Energy Mater* **2020**, *10* (1), 1902573. https://doi.org/10.1002/aenm.201902573.

- (66) Yu, S.; Li, B.; Jiang, J.; Liu, X.; Hao, S.; Han, S.; Yan, W.; Xin, H. Solution-Processed Chalcopyrite Solar Cells: The Grain Growth Mechanism and the Effects of Cu/In Mole Ratio. *Adv Energy Mater* **2022**, *12* (6), 2103644. https://doi.org/10.1002/aenm.202103644.
- (67) Hegedus, S. S.; Shafarman, W. N. Thin-Film Solar Cells: Device Measurements and Analysis. *Progress in Photovoltaics: Research and Applications* **2004**, *12* (23), 155–176. https://doi.org/10.1002/pip.518.
- (68) Nishimura, T.; Toki, S.; Sugiura, H.; Nakada, K.; Yamada, A. Effect of Cu-Deficient Layer Formation in Cu(In,Ga)Se2 Solar-Cell Performance. *Progress in Photovoltaics: Research and Applications* **2018**, *26* (4), 291–302. https://doi.org/10.1002/PIP.2972.
- (69) Nishimura, T.; Toki, S.; Sugiura, H.; Nakada, K.; Yamada, A. Interfacial Quality Improvement of Cu(In,Ga)Se2 Thin Film Solar Cells by Cu-Depletion Layer Formation. *Applied Physics Express* **2016**, *9* (9), 092301. https://doi.org/10.7567/APEX.9.092301/XML.
- (70) McGott, D. L.; Muzzillo, C. P.; Perkins, C. L.; Berry, J. J.; Zhu, K.; Duenow, J. N.; Colegrove, E.; Wolden, C. A.; Reese, M. O. 3D/2D Passivation as a Secret to Success for Polycrystalline Thin-Film Solar Cells. *Joule* 2021, 5 (5), 1057–1073. https://doi.org/10.1016/j.joule.2021.03.015.
- (71) Shah, J. M.; Li, Y.; Gessmann, T.; Schubert, E. F. Experimental Analysis and Theoretical Model for Anomalously High Ideality Factors (N>2.0) in AlGaN/GaN p-n Junction Diodes. *J Appl Phys* **2003**, *94* (4), 2627–2630. https://doi.org/10.1063/1.1593218.
- (72) Keller, J.; Pearson, P.; Shariati Nilsson, N.; Stolt, O.; Stolt, L.; Edoff, M. Performance Limitations of Wide-Gap (Ag,Cu)(In,Ga)Se 2 Thin-Film Solar Cells. *Solar RRL* **2021**, *5* (9), 2100403. https://doi.org/10.1002/solr.202100403.
- (73) Scheer, R.; Schock, H. Appendix A: Frequently Observed Anomalies. In *Chalcogenide Photovoltaics*; Wiley, 2011; pp 305–314. https://doi.org/10.1002/9783527633708.ch7.
- (74) Kim, Y.; Mitzi, D. B. Growth and Photovoltaic Device Application of Cu 2 BaGe 1– x Sn x Se 4 Films Prepared by Selenization of Sequentially Deposited Precursors. *ACS Appl Energy Mater* **2021**, *4* (10), 11528–11536. https://doi.org/10.1021/acsaem.1c02259.
- (75) Müllejans, H.; Wagner, T.; Merli, F.; Jäger-Waldau, A.; Dunlop, E. D. Changes in Spectral Response with Temperature and Irradiance Intensity. *Thin Solid Films* **2004**, *451–452*, 145–151. https://doi.org/10.1016/j.tsf.2003.11.006.

Supplementary Information

Carbon Impurity Minimization of Solution-Processed, Thin-Film Photovoltaics via Ligand Engineering of CuInS₂ Nanoparticles

Daniel C. Hayes, Samantha A. Langdon, Robert M. Spilker, Rakesh Agrawal*

Davidson School of Chemical Engineering, Purdue University, West Lafayette, IN, USA

*Corresponding author: agrawalr@purdue.edu

Experimental Details – Nanoparticle Syntheses

Ink Preparation

All nanoparticle syntheses and precursor preparation steps were performed in a nitrogenfilled glovebox or in a sealed vessel that contained a nitrogen or argon headspace unless otherwise noted. CuCl₂, InCl₃, GaCl₃, InI₃, and GaI₃ precursors were fully dissolved in NMP before use. CuI slurries were also prepared in NMP. Stock solutions of these mixtures were prepared at a concentration of 0.8 M. Cu₂S and In were fully dissolved separately in a PA/EDT stock solution first by adding EDT at a 3:1 and 5:1 EDT:metal ratio, respectively. The mixtures were then diluted with PA to achieve a ~4:1 PA:EDT ratio at a 0.8 M metals concentration. The metal chloride and iodide salts (excluding CuI) usually dissolved within a few hours, but were left to stir overnight to ensure complete dissolution before use in nanoparticle syntheses. Cu₂S usually dissolved within a few hours, while In took one to two days to fully dissolve due to its slower, reactive pathway.¹ Metal acetylacetonate salts (Cu(acac)₂ and Ga(acac)₃) were added directly to the reaction vessel with OLA. At room temperature, attempted dissolutions in OLA at 0.8 M resulted in gelling or incomplete dissolution. Adding directly to the reaction flask ensured that all precursor material was added and was able to dissolve in OLA at elevated temperatures. Stock solutions of sulfur were dissolved in PA or OLA at a concentration of ~1.6 M. Dissolution in PA only took a few hours, but took at least a day in OLA at room temperature. The OLA-acac reaction was the only instance S was added from an OLA-S solution. All inks were dissolved in a 4 mL glass scintillation vial at room temperature with a small PTFE stir bar at a stir rate of 300 RPM. Most of the following reactions were performed using a Biotage Initiator EXP 400 W microwave (MW) reactor for 90 min at 250 °C with a small PTFE stir bar at a stir rate of 600 RPM, unless otherwise noted.

$Cu(In_{1-x}Ga_x)S_2$ Nanoparticle Synthesis – Standard Protocol

 $Cu(In_{1-x}Ga_x)S_2$ (CIGS) nanoparticles (NPs) were synthesized from either metal chlorides and elemental sulfur, or pure metals and metal chalcogenides dissolved in the amine-thiol solvent system. For a typical nanoparticle synthesis with the metal halides and sulfur for x = 0 (i.e., no Ga), 0.29 mmol of $InCl_3$, 0.26 mmol of $CuCl_2$, and 0.86 mmol of S from prepared solutions were added to a borosilicate glass, microwave reaction vessel and diluted to 5 mL total volume with NMP. In order to vary x, the ratio of the indium and gallium precursors was adjusted appropriately while keeping the same IIIA metal concentration accordingly. Nanoparticles synthesized with the amine-thiol system had an In metal concentration of 0.0572 M and a Cu_2S concentration of 0.0257 M, both added from prepared solutions. NMP or OLA were then added for a total reaction volume of 5 mL to 10 mL, depending on whether the reaction was performed in the microwave reactor or

attached to a Schlenk line (SL), respectively, unless otherwise noted. For SL reactions, all reactants were added to a 100 mL three-neck flask with an in-situ thermocouple, stopper, and attached to an Argon-purged Schlenk line via an Allihn condenser. SL reactions with NMP and OLA were performed at 200 °C and 250 °C, respectively, both for 90 min under continuous Ar flow.

For gallium-containing ([Ga]+[In]) (GGI) = 0.3) nanoparticle syntheses using NMP, an In + Ga concentration of 0.0572 M, a [Cu]/([Ga]+[In]) (CGI) ranging from 0.2 to 0.9 and 0.172 M sulfur concentration was prepared from solutions as previously described in a borosilicate glass, microwave reaction vessel and diluted with NMP. This reaction mixture was heated to 250 °C for 90 min. The precursors for this reaction varied between CuCl₂, CuI, InCl₃, InI₃, GaCl₃, and GaI₃. Details regarding the choice of precursor combination will be denoted later in this Supplementary Information section. CIGS nanoparticle reactions with OLA were synthesized via the hot-injection method similar to a previous procedure of ours.² Briefly, a three-neck round bottom flask was prepared in a nitrogen-filled glovebox with 1.75 mmol of Cu(acac)₂, 1.5 mmol of InCl₃, 0.5 mmol Ga(acac)₃, and 12 mL of OLA all added directly to the flask. This flask was then connected to an Argon-purged Schlenk line where it was first heated up to 285 °C. Once the temperature was reached, 6 mL of a 1 M solution of sulfur in OLA was injected into the flask. After injection, the flask was allowed to stir for 30 additional minutes before the heat source was shut off, and the reaction flask was allowed to cool naturally.

Noted Differences Between the Microwave Reactor and Schlenk Line Techniques

As can be seen in the above protocol, nanoparticle reactions were performed either using the solvothermal method with a microwave reactor (MW), or under traditional heat-up conditions using a Schlenk line (SL) and a heating mantle in intimate contact with the reaction vessel. The heating mantles used were fiberglass fabric mantles, sized for 100 mL round-bottom flasks from Glas-Col®, which generated heat via resistive heating. There are two main differences between the two methods:

- 1. The microwave reactor operates under solvothermal conditions, which means reaction vessels were sealed, not allowing any generated vapors to escape. Generated vapors were not believed to negatively affect the nanoparticle products in any way, based on repeated experiments during the preparation of this manuscript. The system is also designed to operate at pressures of up to 20 bar which was used to our advantage when using NMP. NMP has a boiling point of ~202 °C under atmospheric pressure, but in a sealed vessel, we were able to easily perform reactions with NMP up to 250 °C while not even exceeding 5 bar due to the vapor-liquid equilibrium (VLE) achieved between the two phases of NMP in the sealed vessel. Contrarily, reactions in the Schlenk line system were performed under constant Ar flow in an open vessel, thus essentially at atmospheric pressure for the duration of the reaction. This allowed generated vapors to escape, but kept the solvents at their atmospheric boiling points, which prevented us from exceeding much past 200 °C for any reactions performed on the Schlenk line with NMP.
- 2. Due to the different methods of heating between the two systems (microwave radiation vs. resistive heating), the heat-up rates between the two methods were drastically different. This can lead to complications with products (desired or undesired) that require certain kinetic conditions be met to form. The microwave heated up NMP reactions to their set point from room temperature within 2 minutes (microwave radiation is very effective at heating up polar solvents, like NMP), while it took between 20-30 minutes to reach that

same set point with heat-up via resistive heating, used for SL techniques. The main difference noted between the two techniques for a given time and temperature is that MW products generally led to lower FWHM values, indicating higher crystallinity. Based on the results shown in **Figure S1**, the heating rate differences don't appear to be enough to overcome any kinetic barrier favoring between the formation of the wurtzite-phase or chalcopyrite-phase CuInS₂. Rather, for the experiments discussed herein, it is the precursors used, and the decomposition thereof, that favor the formation of one phase over the other.

Table S1. Summary of Selected Solution-Processed CIGSSe Devices via Organic Solution Methods

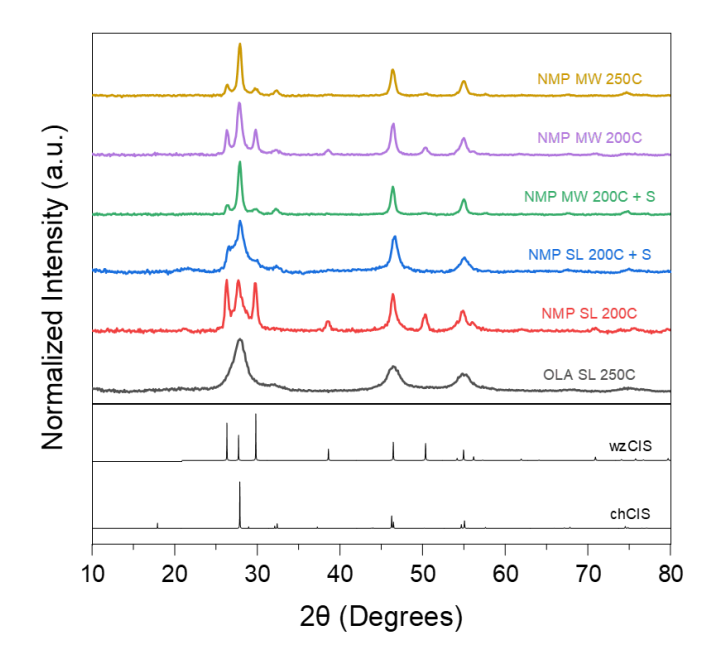
Ref	Rehan et al. (2018) ³	Ahn et al. (2017) ⁴	Rehan et al. (2016) ⁵	Guo et al. (2013) ²
Ink	Hybrid ink – amorphous CISe NPs + molecular solution in 2-MeOEtOH/ H ₂ NEtOH	Hybrid ink – amorphous CISe NPs + molecular solution in 2- MeOEtOH/ H ₂ NEtOH	Cu-In salt precursor – no chalcogen – in 2-MeOEtOH/ H ₂ NEtOH	Colloidal OLA-CIGS NPs in hexanethiol
Alkali Used	Na	Not mentioned	Not mentioned	Na
Selenization	40 Torr N ₂ , 600 °C for 30 min	40 Torr N ₂ , 550 °C for 30 min	40 Torr N ₂ , 560 °C for 30 min	Ar flow, 500 °C for 20 min
FGL Thickness (nm)*	783	1180	513	228
CGL Thickness (nm)*	855	640	692	518
GGI	0	0	0	0.3^{a}
CGI	0.65-0.7 ^b	0.92ª	0.86ª	1 ^a
Eg (eV)	1°	1°	1°	1.2
Jsc (mA/cm ²)	38.59	35.2	33.8	28.8
Voc (V)	0.491	0.46	0.43	0.63
FF (%)	67.74	67	63	65.7
η (%)	12.83 ^{e,y}	10.85 ^{e,z}	9.15 ^{e,z}	12.0 ^{f,z}

Ref	McLeod et al. (2015) ⁶	Yuan et al. (2020) ⁷	Zhao et al. (2021) ⁸	Park et al. (2018) ⁹
Preparation Method	Colloidal OLA- CIGS NPs in hexanethiol	Diamine/dithiol – Dissolution of elemental Cu, In, Ga, Se	Diamine/dithiol – Dissolution of elemental Cu, In, Ga, Se	CIG nitrate salts in MeOH – no chalcogen – with PVA blend
Alkali Used	Na	Not mentioned	Not mentioned	Not mentioned
Selenization	~1 atm Ar, 500 °C for 20 min	N ₂ , 550 °C for 15 min	N ₂ flow, 520 °C for 15 min	 3-step in 2-zone N₂ flow furnace (Se in Z1, sample in Z2): 5 min at 300 °C 35 min at 25 °C, Z1 ramped to 550 °C, Z2 ramped to 400 °C Sample slow ramp to 475 °C, 1% H₂S flow
FGL Thickness (nm)*	130	320	515	282

CGL Thickness (nm)*	860	854	835	595
GGI	0.29 ^b	0.35 ^a	0.35 ^a	0.41 ^a
CGI	0.89^{b}	0.92ª	$0.92^a + 0.7^a$	0.87^{a}
E _g (eV)	1.2	1.21	1.21	1.3-1.5; ~1.1 ^d
J _{SC} (mA/cm ²)	32.1	32.53	33.94	34.73
Voc (V)	0.63	0.65	0.65	0.584
FF (%)	73.4	72.21	73.83	71.00
η (%)	15.0 ^{f,y}	15.25 ^{e,y}	16.39 ^{e,y}	14.4 ^{e,z}

^{*}FGL (fine-grain layer) and CGL (coarse-grain layer) values are average values determined from analyzing SEM cross-section images in ImageJ software.

- a From ink formulation
- $b-Measured \ on \ coated \ or \ selenized \ film$
- c No band gap data provided. Assumed as 1 eV based on no Ga used
- d Authors calculated 1.3-1.5 eV based on SIMS data. Estimate from EQE gives \sim 1.1 eV
- e Active area
- f-Total area
- y MgF₂ ARC deposited
- z No ARC deposited



Sample	FWHM @ 46° (2θ)
NMP MW 250C	0.64
NMP MW 200C	0.64
NMP MW 200C + S	0.57
NMP SL 200C + S	1.01
NMP SL 200C	0.77
OLA SL 250C	1.79

Figure S1. XRD summary of amine-thiol nanoparticle reactions of CuInS₂. Table shows FWHM for the chalcopyrite (204)/(220) or wurtzite (110) reflections for each diffraction pattern. MW denotes reactions performed in the microwave reactor under solvothermal conditions. SL denotes reactions performed on a traditional Schlenk line. Standards used are for the wurtzite-phase CuInS₂ (wzCIS, ICSD# = 163489) and the chalcopyrite-phase CuInS₂ (chCIS, ICSD# = 66865).

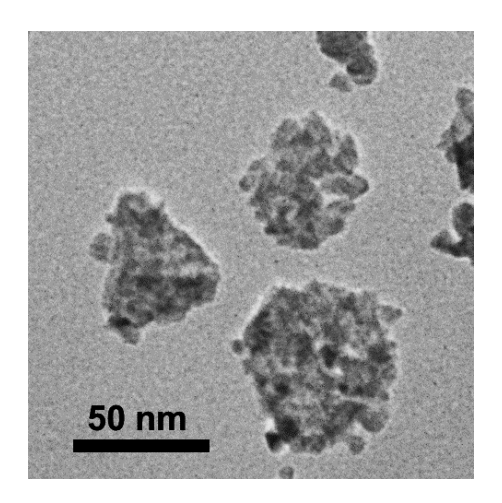


Figure S2. Bright-field TEM image of synthesized NMP-CIS nanoparticles from the CuCl₂, InCl₃, PA-S recipe.

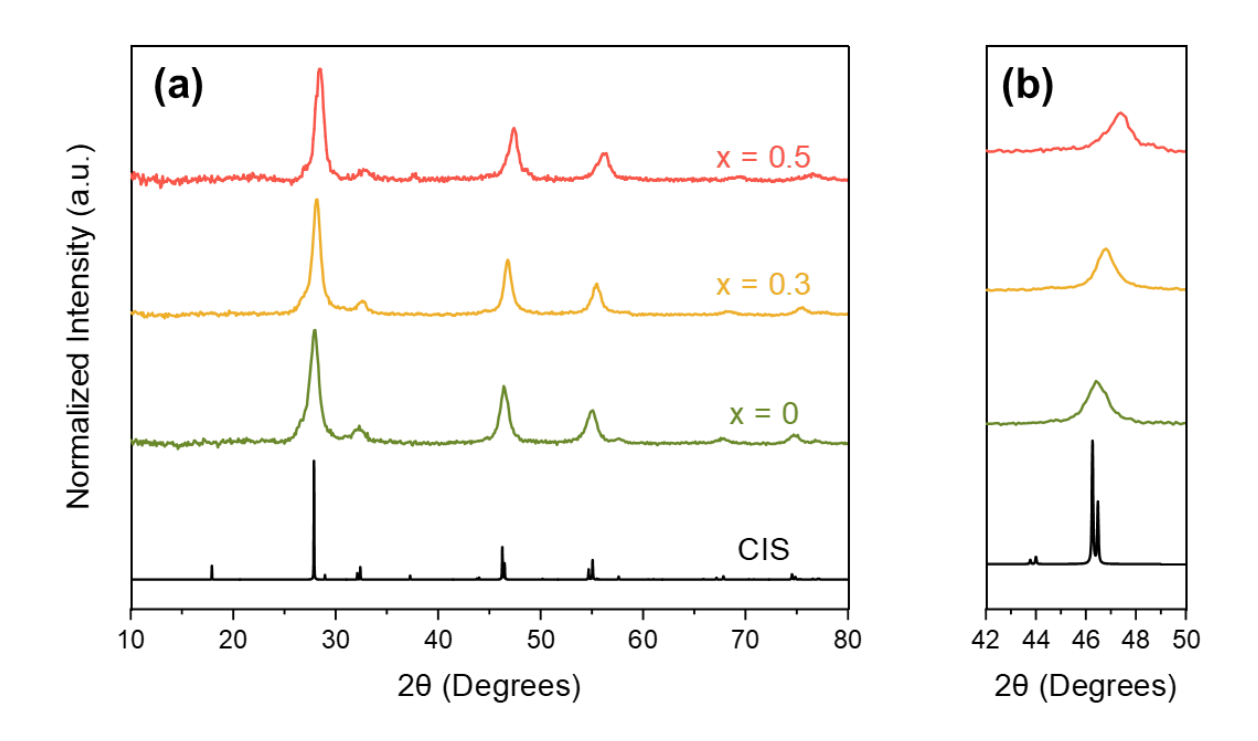


Figure S3. pXRD diffraction patterns of synthesized $Cu(In_{1-x}Ga_x)S_2$ nanoparticles from metal chlroides in NMP. Full spectra (a) and magnification of the chalcopyrite (204)/(220) peaks with a rightward shift in the CIGS samples indicating increasing Ga content (b). Standard used is simulated using VESTA from chalcopyrite $CuInS_2$ - ICSD# 66865.

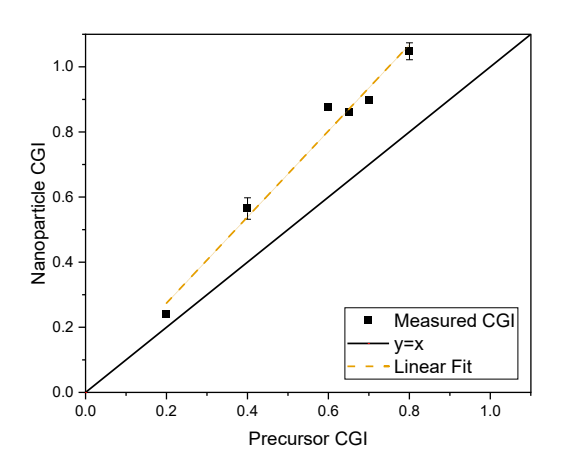


Figure S4. Relation of precursor CGI to synthesized-nanoparticle CGI. Data in this figure were from reactions containing chloride precursors. The gold dashed line is a linear fit to the data. The black solid line is the y = x line. Elemental concentrations were measured using X-ray fluorescence (XRF). These nanoparticles had a target GGI = 0.3.

Difficulties Associated with NMP-CIGS Nanoparticles Synthesized via the NMP Route An additional hurdle that we faced when

An additional hurdle that we faced when synthesizing these nanoparticles was to ensure we obtained an appropriate [Cu]/([Ga]+[In]) (CGI) ratio. CIGS is very tolerant from a stoichiometric standpoint, and the chalcopyrite lattice is able to withstand substantial amounts of Cu vacancies before segregating into different phases. 10 These Cu vacancies are extremely important in CIGS standpoint of the material's optoelectronic properties as they give the material its p-type character, but there exists an optimal CGI for a number of reasons. For one, if the CGI is greater than 1, phase segregation will occur to form stoichiometric CIGS alongside a Cu_{2-x}Se phase. This copper selenide phase is a very conductive species where even a small presence in the absorber layer can overtake the diode characteristics of the solar cell, deteriorating device performance as the CGI continues to increase.¹¹ Too low of a Cu-content can also cause type inversion where the CIGS material switches

from p-type to n-type¹² which would render a CIGS device useless in its standard CIGS/CdS architecture.

For understanding how to control the CGI of these nanoparticles during syntheses, we performed several experiments adjusting the CGI of the added precursors. During these experiments, precursors were tuned to a [Ga]/([Ga]+[In]) (GGI) of 0.3. In **Figure S4**, it can be seen that synthesized nanoparticle CGI deviates from that of the added precursors to the reaction. One thought for these observed results is in regard to the affinity for the cations and anions as they bind to each other in their precursor state as described by Hard-Soft Acid-Base (HSAB) theory. HSAB theory lumps molecular species and several compounds into hard or soft acids or bases depending on the polarizability of the species. Hard species are those that are weakly polarizable, with a typical example being a species that is in a high oxidation state with a small ionic radius. Soft species are those that are highly polarizable, typically comprising of species in a low oxidation state with a large ionic radius. Additionally, HSAB theory also states that alike species bind more strongly to each other, so a hard acid is likely to bind more tightly with a hard base, and similarly with soft acids and soft bases. Likewise, pairings between hard acids and soft bases, and vice versa, are presumed to exhibit weaker bonding. ^{13,14} Under the theory, typical considerations for these species are listed in **Table S2**.

Experiments to test this looked at using metal iodide salts as alternative precursors. The iodide anion is considered a soft base due to its large ionic radius. With a soft base (I⁻) instead of a hard base (Cl⁻), it was presumed that this would allow the In and Ga to more favorably dissociate from the I⁻ anion. Additionally, it was thought that the reactivity of the CuI precursor would be lower by decreasing its dissociation potential. Doing so, however, showed that replacing the anion

with the iodide species had little to no effect at decreasing the CGI ratio of the synthesized nanoparticles (not shown).

In addition to the Cu-content discrepancies, we also experienced colloidal stability issues when synthesizing Gallium-containing, CIGS, nanoparticles via the NMP method. In order to fabricate a smooth nanoparticle-based film—necessary for high-quality thin films—nanoparticle stability is of utmost importance. As described in the introduction of the main text, stable nanoparticle suspensions require a high degree of surface passivation of the nanoparticle—provided by the ligand—and a solvent that allows for a high degree of solvation of the ligand species. These are simultaneously required to reduce surface energies enough to prevent particle agglomeration and flocculation. If one of these is not achieved, nanoparticles will readily cluster and sediment. Trying to coat from such an ink will lead to films with increasing roughness and heterogeneity as the degree of sedimentation increases.

A thorough analysis was not performed on the CIGS nanoparticles as to why they were more prone to sedimentation. Comparison of the XRD patterns between CIS and CIGS nanoparticles show no drastic differences in FWHM (not shown here), indicating that no substantial differences in crystallinity or crystal size are present. Instead, our current theory is that NMP is not able to bind as favorably to the particle surfaces when Ga is introduced. Although propylamine (PA) is shown in **Figure 2** to act as a co-ligand to CIS nanoparticles, we believe the issue to be originating from NMP as PA and oleylamine (OLA) should share the same binding motif and OLA has been shown in previous literature to work well as a ligand for CIGS nanoparticles. This could indicate that PA contributes as a surface ligand to a minority of binding sites, but further study of these stability problems is needed to elucidate this theory.

Table S2. HSAB Considerations for CIGS Metal Precursors

Species	Cu ⁺	Cu ²⁺	In ³⁺	Ga ³⁺	Cl
HSAB Type	Soft	Borderline	Hard	Hard	Hard/Borderline

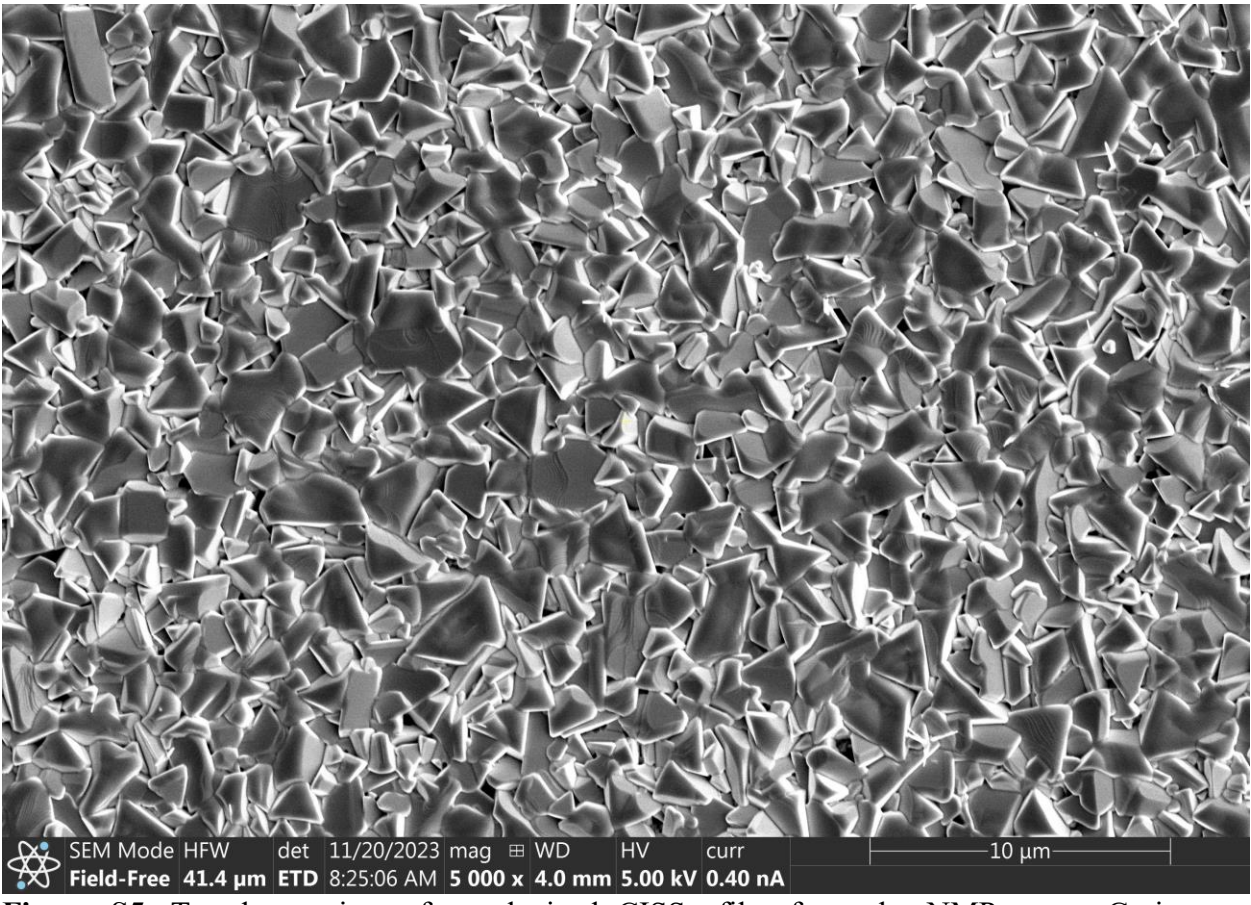
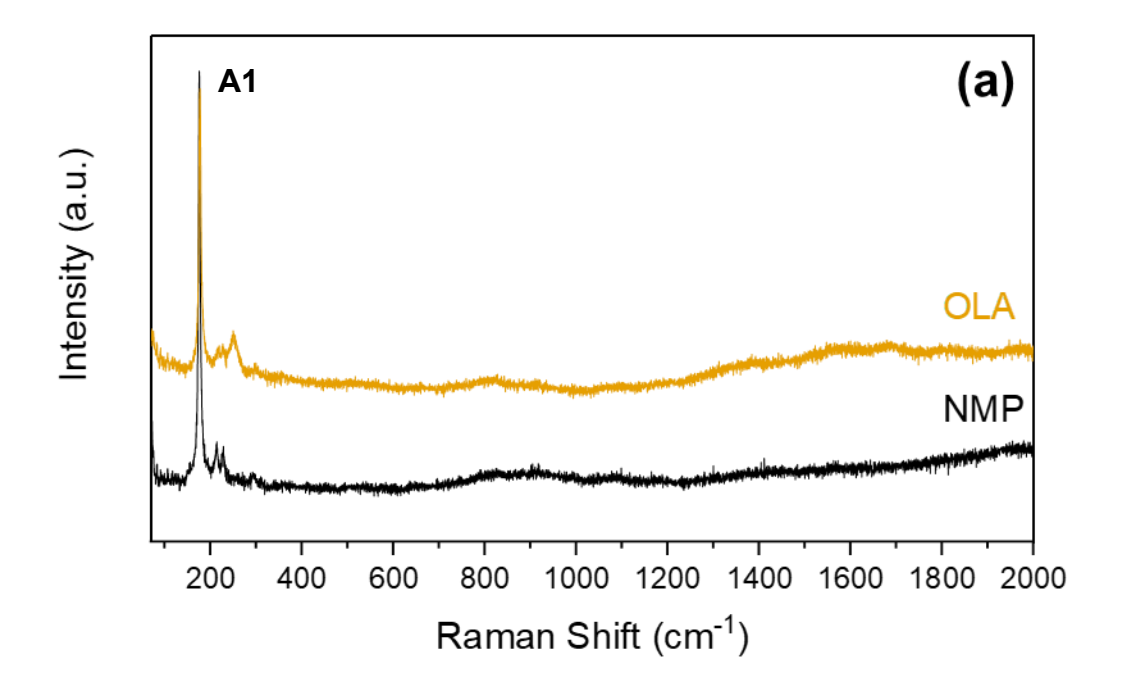


Figure S5. Top-down view of a selenized CISSe film from the NMP route. Grains are predominantly triangular and a bit rigid in structure with small pinholes that are present in the film indicating grain morphology could be improved with a slight increase in Cu-content and optimization of the selenization procedure.



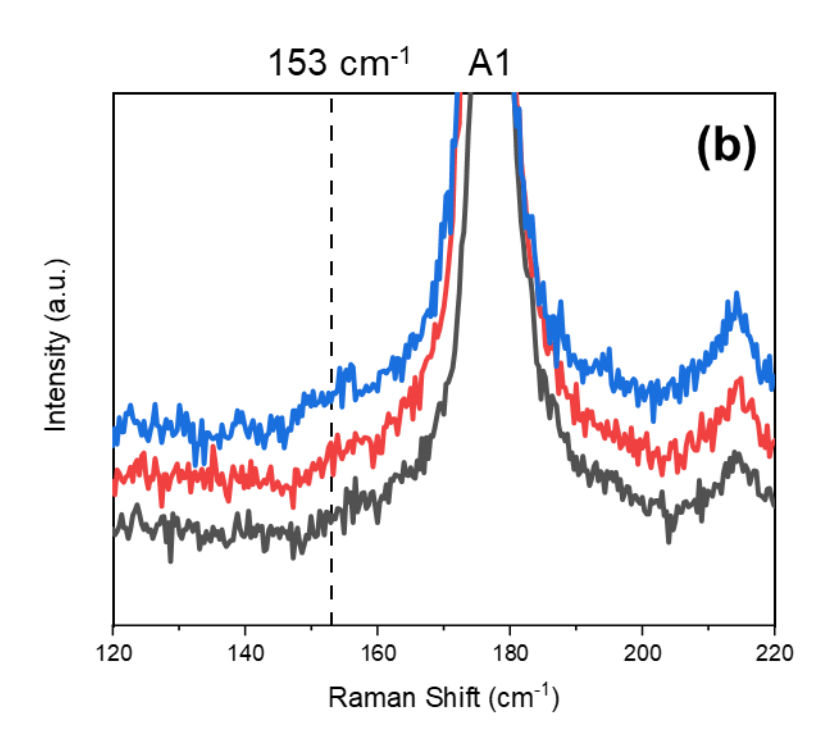


Figure S6. Raman spectra of coarse grains in OLA and NMP films taken by probing the top of the selenized film before any liftoff procedure was performed (a). Very similar responses between the two films indicates the necessity of performing the epoxy-liftoff procedure to probe the fine-grain

layer. Formation of OVC suggested by small shoulder to the left of the main A1 peak (b) in three different samples prepared by the NMP method under the same conditions.

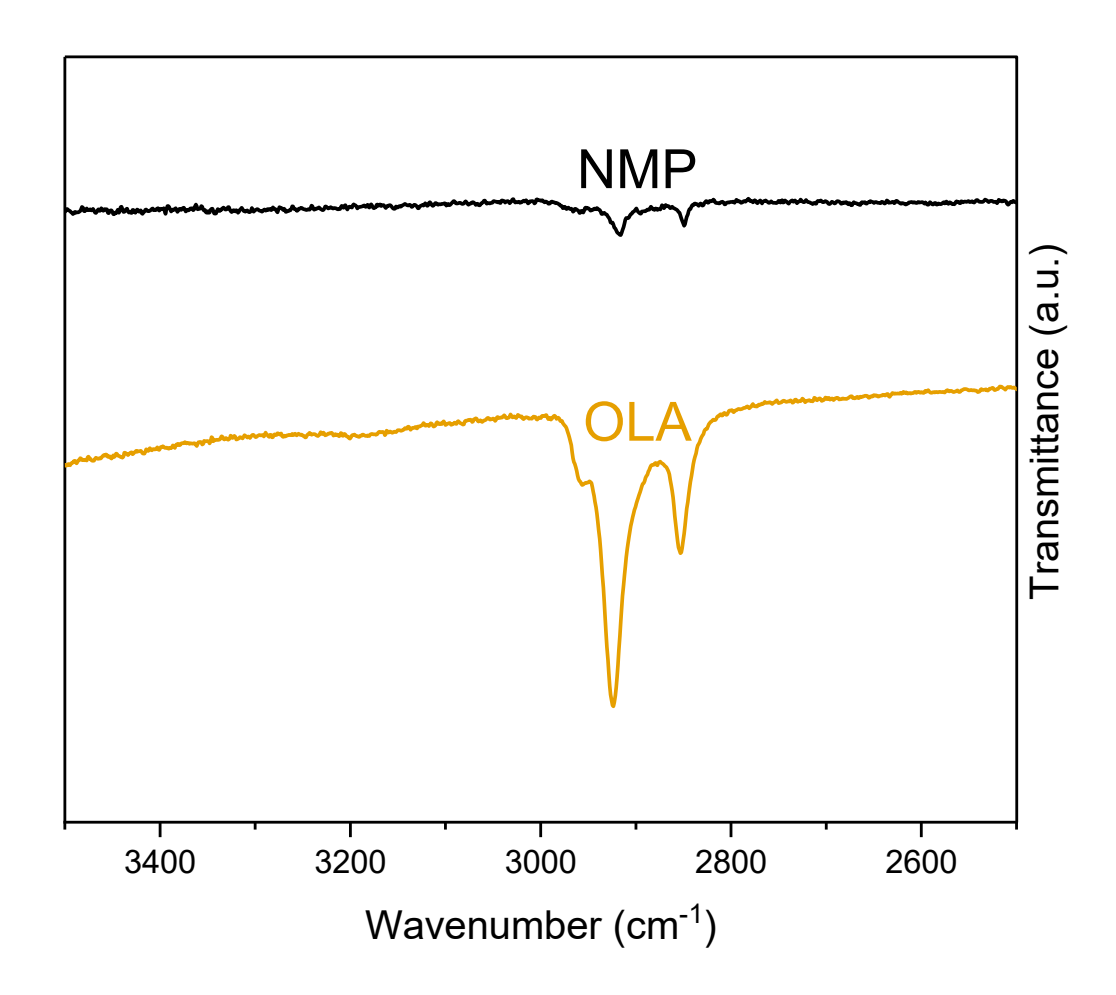


Figure S7. Infrared spectroscopy of coated and annealed films (before selenization) of nanoparticles synthesized from the NMP route and the OLA route. The OLA route shows much more intense response in the 2800-3000 cm⁻¹ signal due to more C-H stretching from the increased C-H moieties in OLA, and thus, increased carbon content from the OLA route.

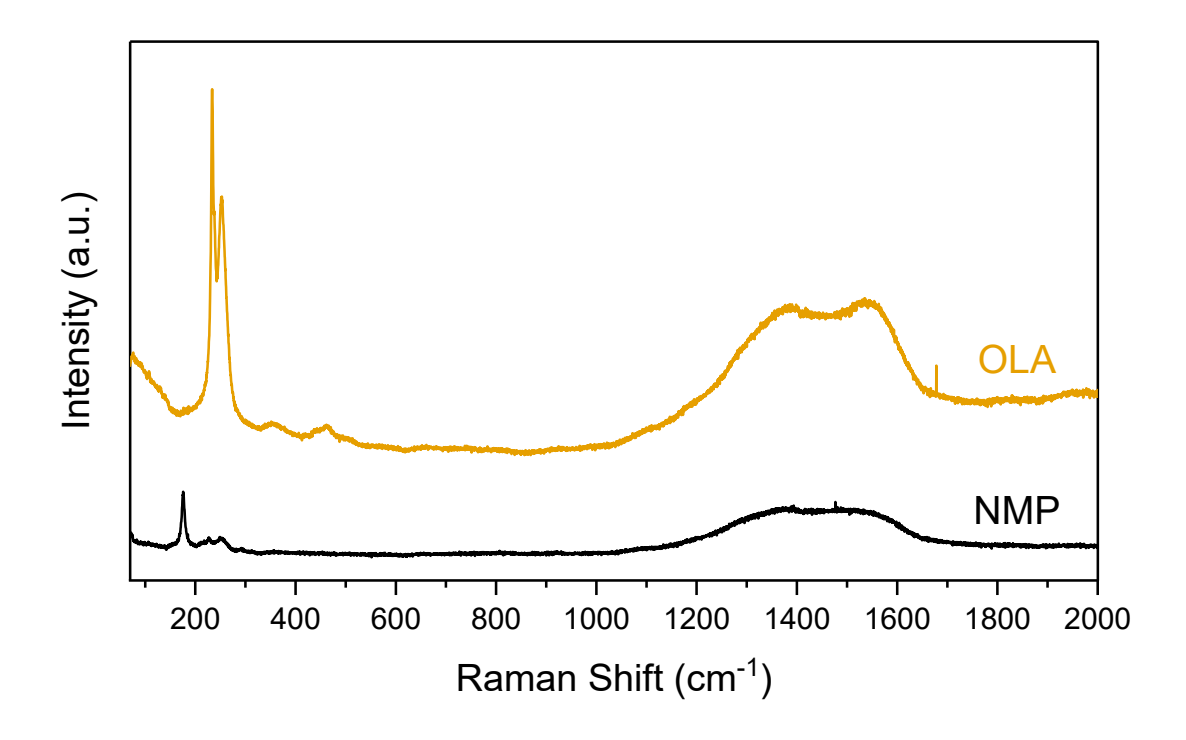


Figure S8. Raman spectra of the original substrate of the OLA and NMP films where some film residue remained. This measurement ensures that no laser penetration into the coarse-grain layer is occurring, and thus should probe ONLY the fine-grain layer. Much like **Figure 5** in the main text, we see a similar pattern with lower carbon content as well as increased chalcopyrite character in the NMP film. In the OLA film, we don't see any visible chalcopyrite resonances, rather those only from Se and carbon. The reader should note that while these two spectra were taken with the same excitation parameters, it is unclear how differences in the thickness of the probed layer affected these results. Thus, we interpret this figure only by observing relative differences in intensities, specifically the difference between the chalcopyrite A1 peak (~175 cm⁻¹) and the carbon peaks (~1200-1700 cm⁻¹).

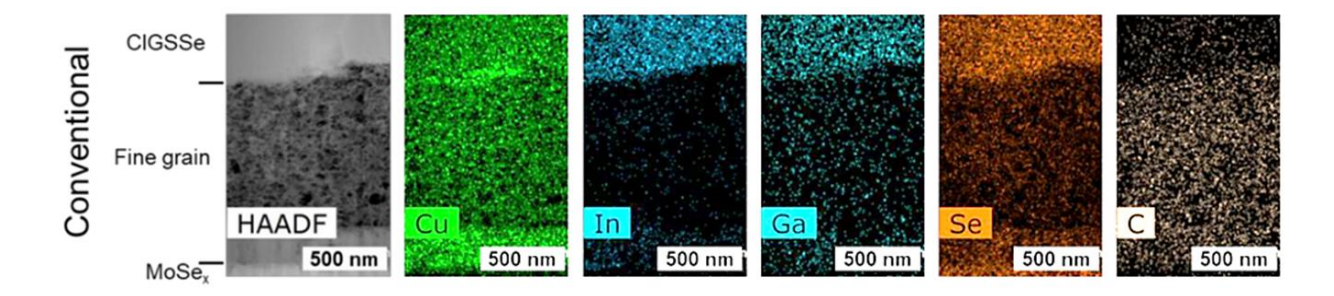


Figure S9. STEM-EDS of the residual unsintered layer, or fine-grain layer, after selenization of a conventional OLA-capped nanoparticle film. Adapted with permission. Copyright 2020, American Chemical Society.

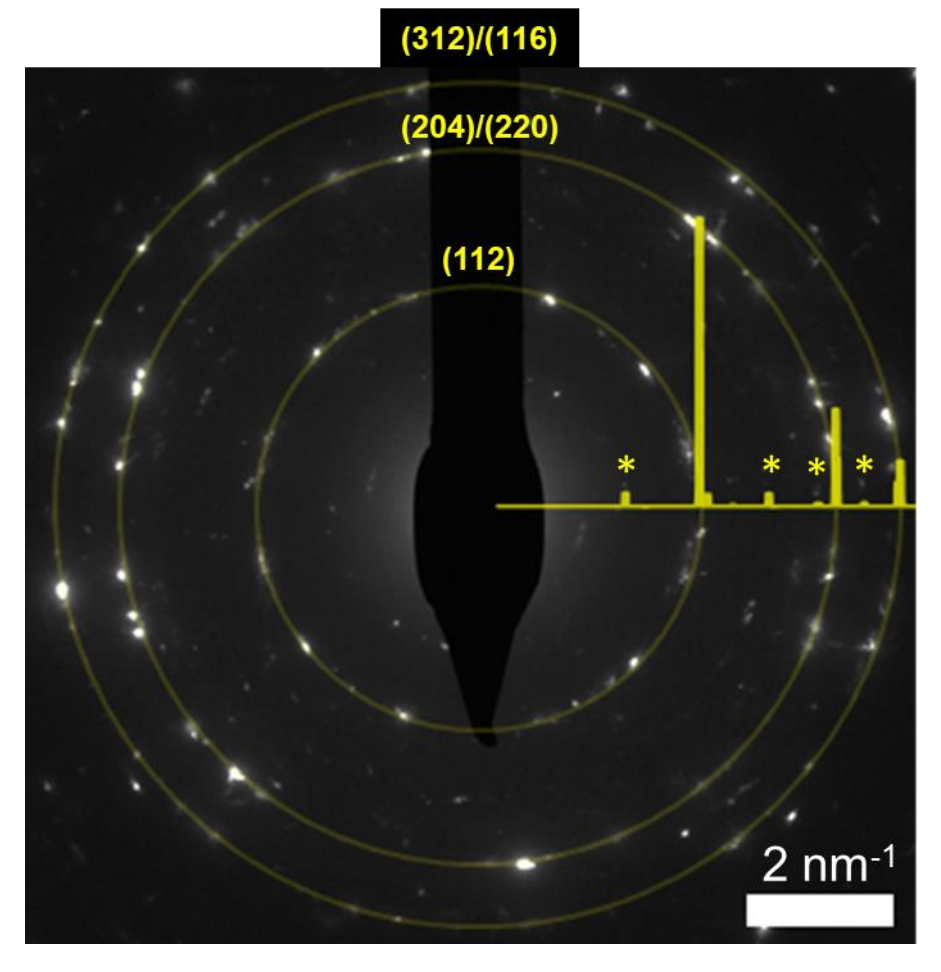


Figure S10. Selected area electron diffraction (SAED) pattern of the fine-grain layer of the FIBed sample indicating the presence of chalcopyrite CuInSe₂ within the fine-grain layer. Yellow diffraction pattern is the CuInSe₂ standard (ICSD# 73351) with yellow rings shown as a visual aid to help distinguish diffraction rings. While some of the other diffraction spots appear to belong to the lower-intensity reflections of CISe (marked with *), EDX revealed that a Cu-Se phase exists within the fine-grain layer from which other diffraction spots may belong to.

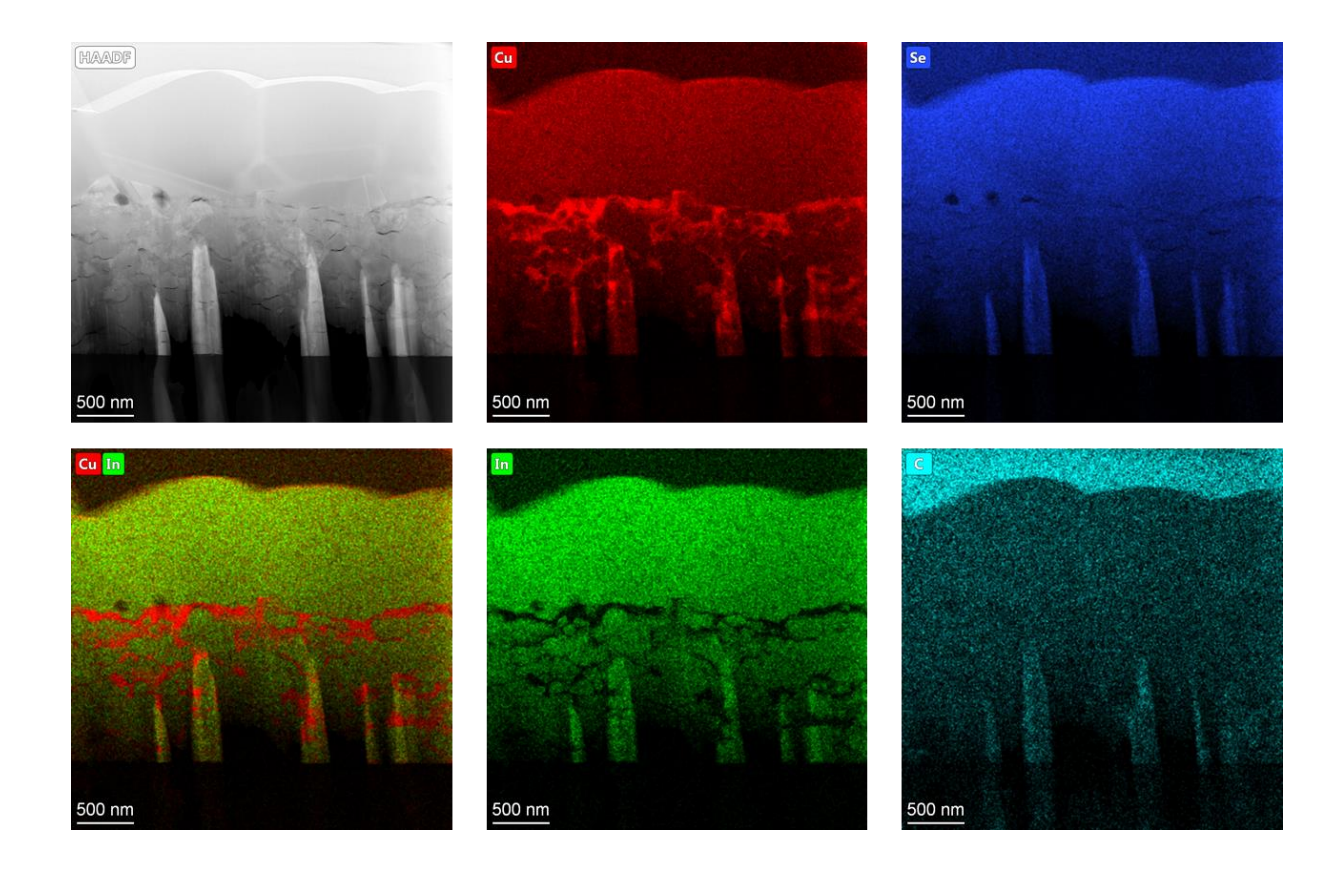


Figure S11. EDX intensity maps of the full sample measured via STEM. Distinguishable are the Cu veins in the fine-grain region, as described in the main text and that the C content appears largely homogeneous across the depth of the film. The bright streaks in each of the images are curtaining artifacts from the etching process of the focused-ion beam (FIB). The dark region below the film which shows little to no counts is the soda-lime glass upon which the sample was coated. The C-rich layer on top of the film is due to Pt deposition during the FIB session which is deposited by a carbon-containing carrier gas.

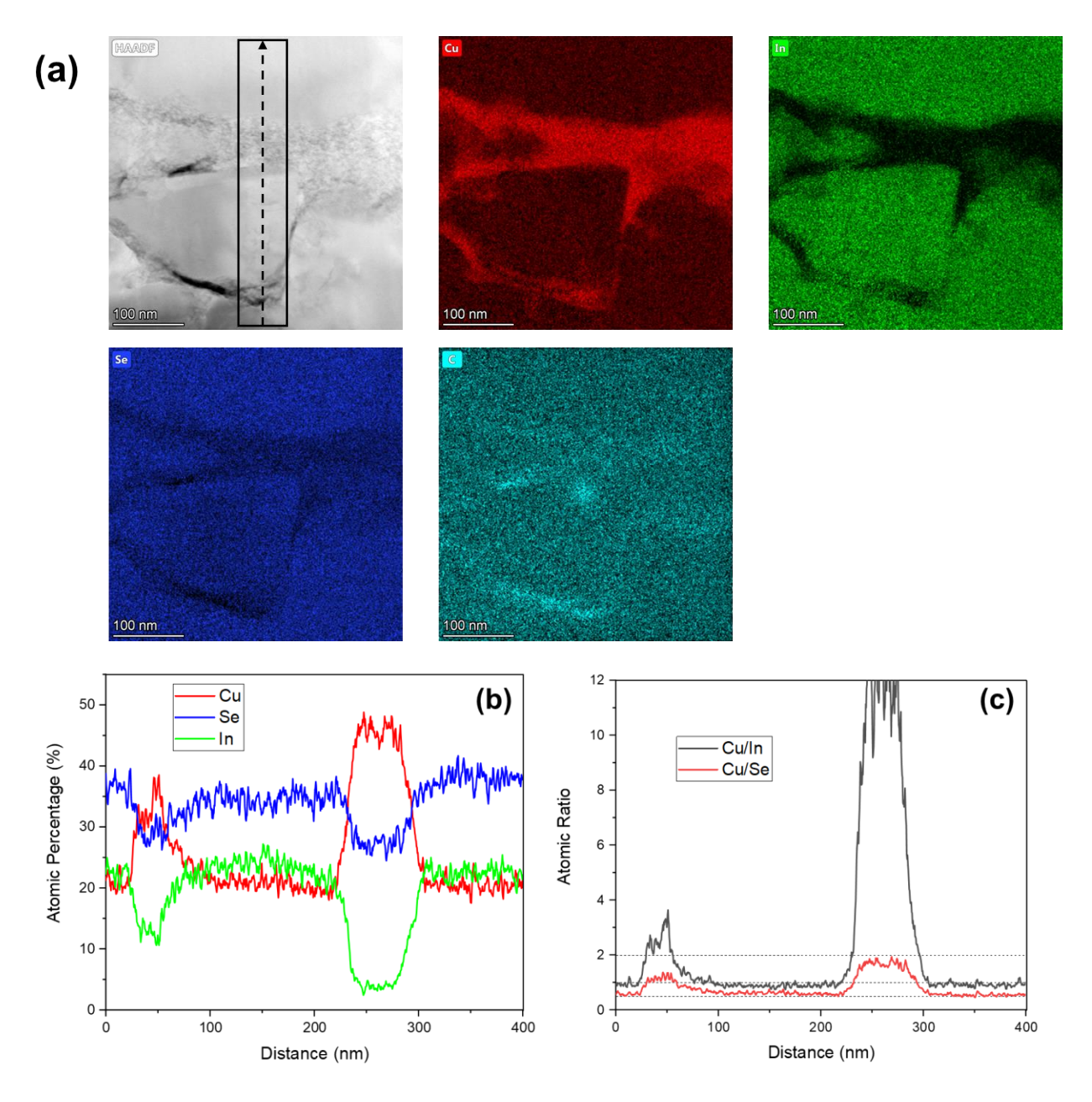


Figure S12. STEM-EDX atomic percentage maps of a Cu-vein in the fine-grain region (a) with data from the line scan in (b)—line scan range is illustrated in the HAADF image of (a)—and the Cu/In and Cu/Se ratios from the line scan are shown in (c). The grain in the upper third of the image is among the coarse grains. The higher intensity spot in the center of the C map is due to the beam spot being centered in the view plane, causing accumulation of carbon contamination induced by the electron beam. Note that there appear to be regions of high C content in the C map. These maps are atomic % maps, and the apparent high C areas are associated with holes in the FIB sample (as seen by the black spots in the HAADF image) where not much material is present. Notable from (c) is that the Cu/In ratio is predominately unchanged between CISe grains in the coarse-grain region and that of the fine-grain region.

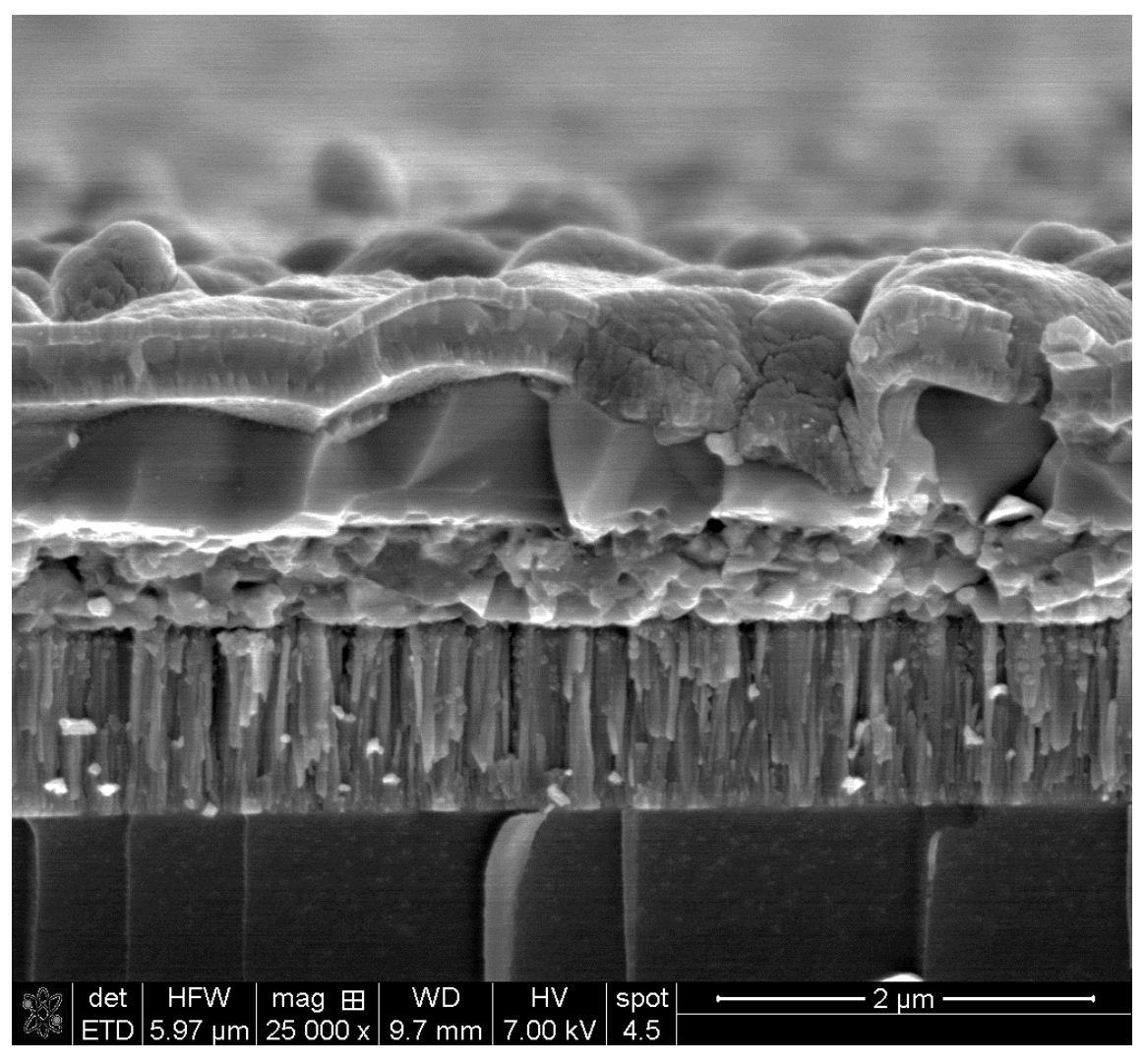


Figure \$13. Cross-section SEM image of a completed CISSe device.

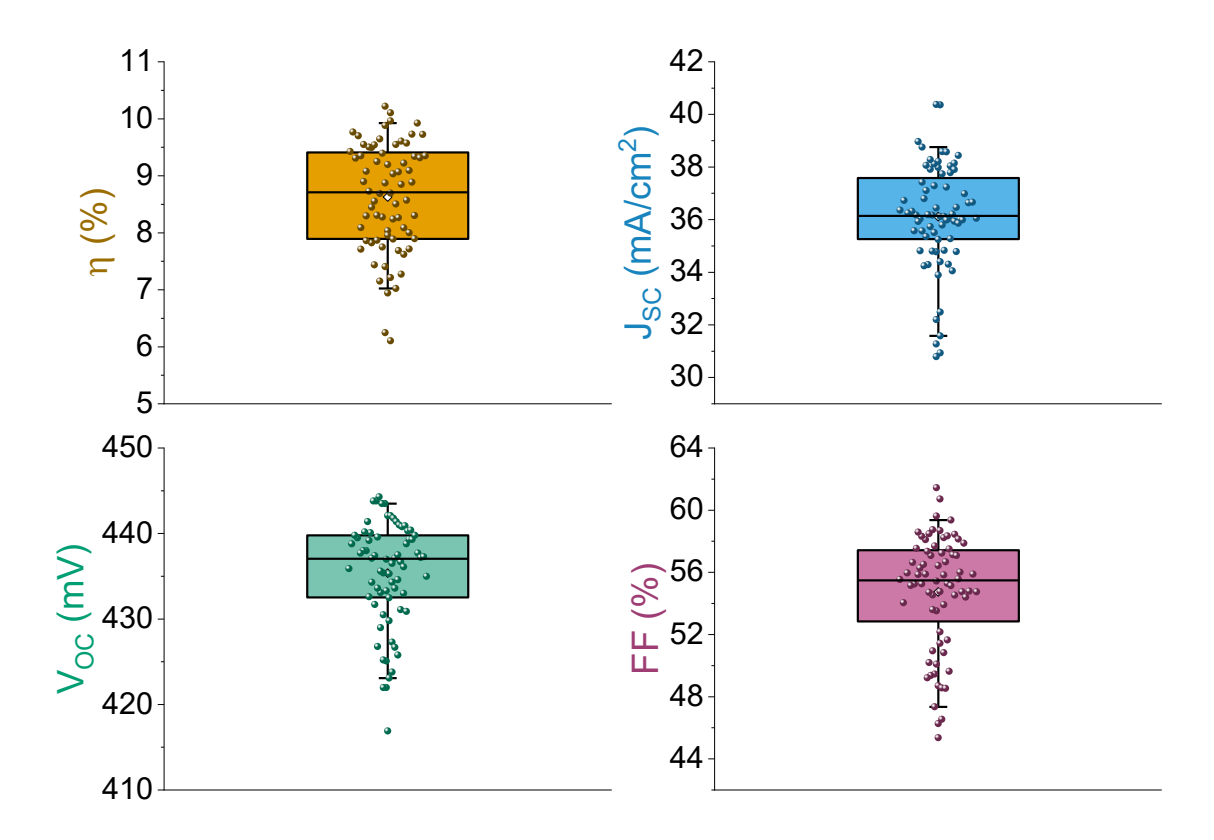


Figure S14. Box plots from JV analyses of 35 devices measured for this study. Data in this figure are from devices without a MgF₂ anti-reflective coating. The large spread for the data points, such as with the J_{SC}, are likely due to the non-optimized selenization conditions used for experiments performed during preparation of this manuscript. Additionally, local differences in Se partial pressure can greatly impact the amount of Se that condenses on the film during selenization, altering the grain growth process and affecting the properties and morphology of the resulting film.

Derivation of Device Parameters

To derive the device parameters R_{sh} , R_s , n, and J_0 , the following equation for a single-diode model was used

$$J(V) = J_0 \left[\exp\left(\frac{q(V - JR_s)}{nkT}\right) \right] + \frac{V}{R_{sh}} - J_L$$
 (1)

and the Shafarman method was followed¹⁶ where J is the measured current density, J_0 is the saturation current, q is the elementary charge, V is the voltage input from the voltage sweep, R_s is the series resistance, n is the diode ideality factor, k is the Boltzmann constant, T is the absolute temperature, R_{sh} is the shunt resistance, and J_L is the light-generated current. All parameters in Table 1 in the main text were calculated from the light curve. All values were determined graphically via linear fits by modifying (1) as follows:

$$\left. \frac{dJ}{dV} \right|_{V=0} \approx \frac{1}{R_{Sh}}$$
 (2)

$$\frac{dV}{dJ} = \frac{nkT}{q} \left[\frac{1 - \left(\frac{dV/dJ}{R_{sh}}\right)}{J + J_L - \frac{V}{R_{sh}}} \right] + R_s \tag{3}$$

$$\ln\left(J + J_L - \frac{V}{R_{sh}}\right) = \ln(J_0) + \frac{q}{nkT}(V - JR_s) \tag{4}$$

Where R_{sh} was solved with (2), R_s and n were solved with (3), and J_0 was solved with (4). When solving for the parameters, we set $J_L = J_{SC}$ when analyzing the light curve, and $J_L = 0$ for the dark curve. Dark curve values are shown in **Table S3**, below. The only observable differences between dark and light parameters is in the R_{sh} and J_0 terms which may be due to some slight voltage dependence of the light-induced current.

Table S3. Dark J-V Parameters for the Champion Solar Cell

R _{sh,dark} (Ω cm ²)	$R_{s,dark} (\Omega cm^2)$	n	J ₀ (mA/cm ²)
490	1.09	2.1	2.28×10 ⁻³

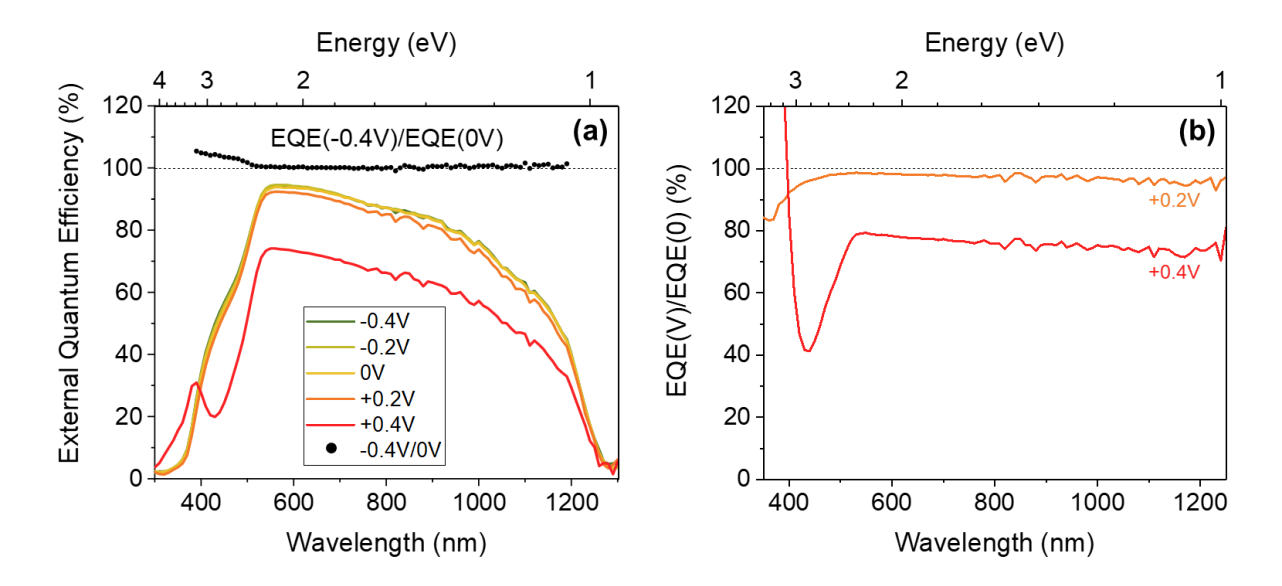


Figure S15. Voltage-dependent EQE is shown for the champion device at biases of $0, \pm 0.2$, and ± 0.4 V. The ratio of the -0.4 V biased EQE and the non-biased EQE is shown with black spheres (a). Ratio of biased EQE to non-biased EQE (b).

Another note for **Figure S15a** is the increase in collection below 400 nm in the +0.4 V bias scan. This has typically been attributed to enhanced photoconductivity of the CdS layer, caused by trapping of light-generated holes into ionized deep acceptor states in the CdS layer, and is an effect typically only observed in "dark" EQE measurements (where no external light biasing is applied) at high forward biases where the diode current begins to dominate the device. ^{17,18}

We consider surface recombination to be the dominating recombination pathway based on the apparent shift in the values of the ratios shown in **Figure S15b** from $\lambda > \sim 540$ nm. Although the slope of the data is very small, the slight negative slope may imply some bulk recombination effects are present as well. Deviations from this behavior, such as the minima located at ~ 430 nm for the +0.4V bias spectra and the spike at lower wavelengths, are caused by the CdS photoconductivity, as previously discussed.

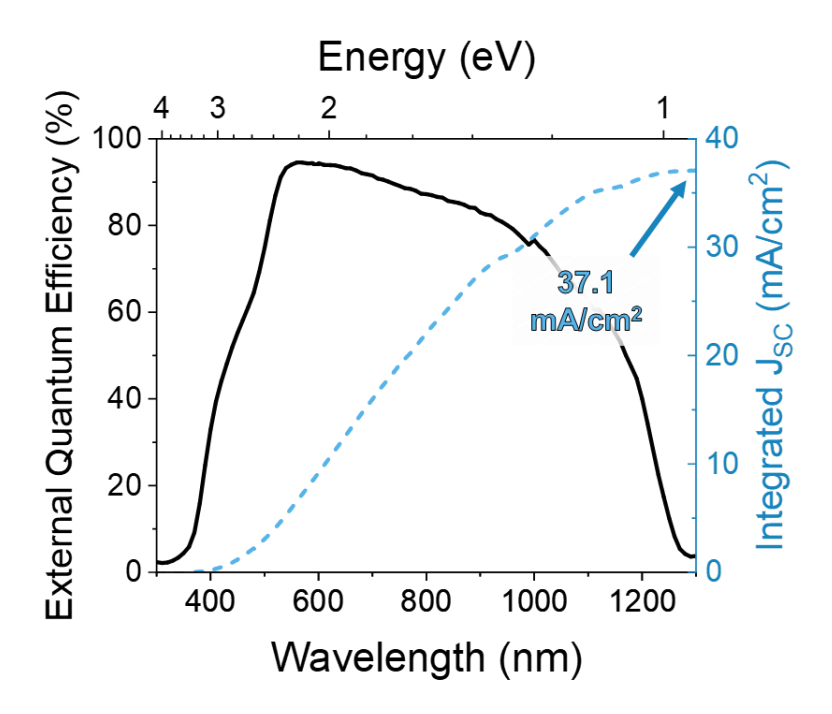


Figure S16. Integrated short-circuit current density calculated from the champion device EQE spectrum. $J_{SC,EQE}$ was calculated using

$$J_{SC,EQE} = \frac{q}{hc} \int_{0}^{\infty} \lambda A M_{1.5G}(\lambda) EQE(\lambda) d\lambda$$

Where q, h, and c are the elementary charge, Planck constant, and speed of light with values of 1.609E-19 C, 6.626E-34 J*m, and 2.998E8 m/s, respectively. λ , AM_{1.5G}(λ), and EQE(λ) are in nm, W/m²/nm, and unitless, respectively.

Apparent EQE

As discussed in the main text, our EQE data reads as having a slightly positive quantum efficiency at the extreme wavelengths. *This observation was made even after several repeat measurements*. The raw data output during these measurements (not shown here)—before manipulating with the calibration data—is measured by the system as current. For the raw sample data, current readings were negligible at the extremes, indicating no significant absorption of light by the samples at those wavelengths. Since there is no white light bias during these measurements, and since the absorption is also inherently small for both the Si and Ge calibration standards at the extremes, the current produced by each is extremely small, which can lead to larger calculation errors at the extreme ends of the spectrum, thus producing what appears to be a small, positive quantum efficiency. The apparent quantum efficiency from the extremes attributes to <0.1 mA/cm² towards the integrated J_{SC,EOE}.

References:

- (1) Zhao, X.; Deshmukh, S. D.; Rokke, D. J.; Zhang, G.; Wu, Z.; Miller, J. T.; Agrawal, R. Investigating Chemistry of Metal Dissolution in Amine–Thiol Mixtures and Exploiting It toward Benign Ink Formulation for Metal Chalcogenide Thin Films. *Chemistry of Materials* **2019**, *31* (15), 5674–5682. https://doi.org/10.1021/acs.chemmater.9b01566.
- Guo, Q.; Ford, G. M.; Agrawal, R.; Hillhouse, H. W. Ink Formulation and Low-Temperature Incorporation of Sodium to Yield 12% Efficient Cu(In,Ga)(S,Se) 2 Solar Cells from Sulfide Nanocrystal Inks. *Progress in Photovoltaics: Research and Applications* **2013**, *21* (1), 64–71. https://doi.org/10.1002/pip.2200.
- (3) Rehan, S.; Moon, J.; Kim, T. G.; Gwak, J.; Kim, J.; Kim, J. W.; Jo, W.; Ahn, S. K.; Ahn, S. Role of Na in Solution-Processed CuInSe2 (CISe) Devices: A Different Story for Improving Efficiency. *Nano Energy* **2018**, *48*, 401–412. https://doi.org/10.1016/j.nanoen.2018.03.065.
- (4) Ahn, S.; Rehan, S.; Moon, D. G.; Eo, Y.-J.; Ahn, S.; Yun, J. H.; Cho, A.; Gwak, J. An Amorphous Cu–In–S Nanoparticle-Based Precursor Ink with Improved Atom Economy for CuInSe 2 Solar Cells with 10.85% Efficiency. *Green Chemistry* **2017**, *19* (5), 1268–1277. https://doi.org/10.1039/C6GC03280J.
- (5) Rehan, S.; Kim, K. Y.; Han, J.; Eo, Y.-J.; Gwak, J.; Ahn, S. K.; Yun, J. H.; Yoon, K.; Cho, A.; Ahn, S. Carbon-Impurity Affected Depth Elemental Distribution in Solution-Processed Inorganic Thin Films for Solar Cell Application. *ACS Appl Mater Interfaces* **2016**, *8* (8), 5261–5272. https://doi.org/10.1021/acsami.5b10789.
- (6) McLeod, S. M.; Hages, C. J.; Carter, N. J.; Agrawal, R. Synthesis and Characterization of 15% Efficient CIGSSe Solar Cells from Nanoparticle Inks. *Progress in Photovoltaics: Research and Applications* **2015**, *23* (11), 1550–1556. https://doi.org/10.1002/pip.2588.
- (7) Yuan, S.; Wang, X.; Zhao, Y.; Chang, Q.; Xu, Z.; Kong, J.; Wu, S. Solution Processed Cu(In,Ga)(S,Se) 2 Solar Cells with 15.25% Efficiency by Surface Sulfurization. *ACS Appl Energy Mater* **2020**, *3* (7), 6785–6792. https://doi.org/10.1021/acsaem.0c00917.
- (8) Zhao, Y.; Yuan, S.; Chang, Q.; Zhou, Z.; Kou, D.; Zhou, W.; Qi, Y.; Wu, S. Controllable Formation of Ordered Vacancy Compound for High Efficiency Solution Processed Cu(In,Ga)Se 2 Solar Cells. *Adv Funct Mater* **2021**, *31* (10), 2007928. https://doi.org/10.1002/adfm.202007928.
- (9) Park, G. S.; Chu, V. Ben; Kim, B. W.; Kim, D.-W.; Oh, H.-S.; Hwang, Y. J.; Min, B. K. Achieving 14.4% Alcohol-Based Solution-Processed Cu(In,Ga)(S,Se) 2 Thin Film Solar Cell through Interface Engineering. *ACS Appl Mater Interfaces* **2018**, *10* (12), 9894–9899. https://doi.org/10.1021/acsami.8b00526.
- (10) Stanbery, B. J. Copper Indium Selenides and Related Materials for Photovoltaic Devices. *Critical Reviews in Solid State and Materials Sciences* **2002**, *27* (2). https://doi.org/10.1080/20014091104215.

- (11) Marko, H.; Arzel, L.; Darga, A.; Barreau, N.; Noël, S.; Mencaraglia, D.; Kessler, J. Influence of Cu Off-Stoichiometry on Wide Band Gap CIGSe Solar Cells. *Thin Solid Films* **2011**, *519* (21), 7228–7231. https://doi.org/10.1016/J.TSF.2010.12.174.
- (12) Shafarman, W. N.; Siebentritt, S.; Stolt, L. Cu(InGa)Se2 Solar Cells. In *Handbook of Photovoltaic Science and Engineering*; John Wiley & Sons, Ltd, 2011; pp 546–599.
- (13) Coughlan, C.; Ibáñez, M.; Dobrozhan, O.; Singh, A.; Cabot, A.; Ryan, K. M. Compound Copper Chalcogenide Nanocrystals. *Chem Rev* **2017**, *117* (9), 5865–6109. https://doi.org/10.1021/acs.chemrev.6b00376.
- van Embden, J.; Chesman, A. S. R.; Jasieniak, J. J. The Heat-up Synthesis of Colloidal Nanocrystals. *Chemistry of Materials* **2015**, *27* (7), 2246–2285. https://doi.org/10.1021/cm5028964.
- (15) Ellis, R. G.; Turnley, J. W.; Rokke, D. J.; Fields, J. P.; Alruqobah, E. H.; Deshmukh, S. D.; Kisslinger, K.; Agrawal, R. Hybrid Ligand Exchange of Cu(In,Ga)S 2 Nanoparticles for Carbon Impurity Removal in Solution-Processed Photovoltaics. *Chemistry of Materials* **2020**, *32* (12), 5091–5103. https://doi.org/10.1021/acs.chemmater.0c00966.
- (16) Hegedus, S. S.; Shafarman, W. N. Thin-Film Solar Cells: Device Measurements and Analysis. *Progress in Photovoltaics: Research and Applications* **2004**, *12* (23), 155–176. https://doi.org/10.1002/pip.518.
- (17) Hages, C. J.; Carter, N. J.; Agrawal, R. Generalized Quantum Efficiency Analysis for Non-Ideal Solar Cells: Case of Cu2ZnSnSe4. *J Appl Phys* **2016**, *119* (1). https://doi.org/10.1063/1.4939487.
- (18) Gloeckler, M.; Sites, J. R. Apparent Quantum Efficiency Effects in CdTe Solar Cells. *J Appl Phys* **2004**, *95* (8), 4438–4445. https://doi.org/10.1063/1.1667605.